Journal of Advanced Ceramics
先进陶瓷
ISSN 2226-4108
CN 10-1154/TQ
清华大学出版社 Tsinghua University Press
SciOpen

J Adv Ceram 2026, **15**: 9221368

https://doi.org/10.26599/JAC.2026.9221368

Research Article

Strong-bond networks and basal-cleavage resistance govern strength–toughness balance and elevated-temperature retention in Ta-based medium-entropy 211 MAX ceramics

Lu Liu[1], Qifeng Zhuang[1], Xiyu Xiao[2], Wei Ding[1], Haoran Zhou[2], Xuefang Yin[2], Kaicheng Zhang[3], Baoze Zhao[1], Shun Dong[4,*], Guobing Ying[1,3,*]

[1] *Department of Engineering Mechanics, College of Mechanics and Engineering Science, Hohai University, Nanjing 211100, China.*

[2] *College of Materials Science and Engineering, Hohai University, Changzhou 213200, China.*

[3] *School of Materials Science and Engineering, Southeast University, Nanjing 211189, China.*

[4] *National key laboratory of science and technology on advanced composites in special environments, Harbin Institute of Technology, Harbin 150001, China.*

*Corresponding author.

E-mail: S. Dong, dongshun@hit.edu.cn;

G. Ying, gbying@seu.edu.cn

Received: July 7, 2026; Revised: August 20, 2026; Accepted: August 28, 2026

Abstract: Ta-containing MAX phases are promising high-temperature structural ceramics, but high density and concurrent optimization of strength, fracture toughness, and elevated-temperature property retention remains challenging. Entropy engineering can tailor M-site chemistry; however, it remains unclear how M-site combinations control the strength–toughness balance and elevated-temperature retention. Here, $(TaNbV)_2AlC$, $(TaTiNb)_2AlC$, $(TaTiV)_2AlC$, and $(TaTiNbV)_2AlC$ were synthesized by vacuum hot pressing and investigated through phase and microstructural characterization, density functional theory (DFT)-based crystal orbital Hamilton population (COHP) analysis, Deep Potential molecular dynamics (DP-MD), and mechanics-based bridging models. Characterization confirmed a layered M_2AlC-type framework and showed no obvious M-site elemental segregation within the examined regions. Compared with Ta_2AlC, all medium-entropy ceramics showed reduced density and improved room-temperature flexural strength and fracture toughness, with $(TaNbV)_2AlC$ achieving 578 MPa and 8.5 $MPa \cdot m^{1/2}$. COHP revealed stronger M–C and M–Al bonding in Ta/Nb-centered environments than in Ti- and V-centered environments, explaining the flexural-strength grouping. However, fracture toughness required path-dependent basal-cleavage descriptors beyond average bond strength. A validated DP-MD model demonstrated structural retention up to 1500 K under inert (oxygen-free) conditions and within the simulation time scale, intrinsic tensile softening, and composition-dependent cleavage-work retention. Qualitative-to-semiquantitative bridging projections indicate that $(TaNbV)_2AlC$ provides the highest absolute strength and toughness, whereas $(TaTiNbV)_2AlC$ has the best elevated-temperature retention. These results reveal that Ta/Nb-rich bonding and basal-cleavage resistance act as complementary, composition-dependent mechanisms governing the strength–toughness balance and its elevated-temperature retention in this Ta-based 211 MAX series, providing a mechanistic basis for designing entropy-engineered MAX ceramics with room-temperature performance and elevated-temperature property retention as distinct targets.

Keywords: Ta-based MAX ceramics; medium-entropy ceramics; M-site chemistry; strength–toughness balance; basal cleavage; Deep Potential molecular dynamics

1 Introduction

MAX phases, generally formulated as $M_{n+1}AX_n$ (where M is an early transition metal, A is a group 13 or 14 element, X is C and/or N, and n = 1–4), are nanolaminated carbides and nitrides in which transition-metal carbide/nitride slabs are interleaved with A-element atomic layers. The coexistence of strong M–X bonding and comparatively weaker M–A interactions underlies their unusual combination of ceramic-like stiffness, thermal stability, and oxidation resistance with metallic-like machinability, electrical/thermal conductivity, and damage tolerance [1–4]. The compositional space of MAX phases continues to expand, as demonstrated by the prediction and synthesis of new MAX compounds such as V_2SnC and Mo_2Ga_2C, as well as entropy-engineered M_2SnC systems with complex M-site chemistry [5–7]. These characteristics, together with composition-dependent high-temperature oxidation or decomposition pathways that may form protective oxide scales and/or refractory carbide-derived products, have stimulated interest in MAX phases as high-temperature structural materials and protective coatings for severe environments [8–11]. Among them, Ta-containing MAX phases are particularly attractive because Ta–C chemistry is intrinsically refractory, as exemplified by the high melting point of TaC, approximately 3880 °C [12]. However, Ta-rich members also carry a substantial density penalty, which is unfavorable for mass-sensitive high-temperature components [13]. The key materials-design challenge is therefore to retain the refractory and damage-tolerant advantages of Ta-containing MAX chemistry while improving the balance among density, strength, and fracture resistance.

Although bonding anisotropy is a general feature of MAX phases, the M_2AlC-type 211 structure provides a comparatively simple platform for examining how M-site chemistry affects mechanical response. In this structure, changes on the M sublattice can perturb both the strong M–C carbide

network and the weaker M–Al interlayer environment. As a result, M-site chemical design in 211 MAX ceramics may influence stiffness and strength through the carbide framework while also modifying crack propagation and fracture resistance through the layered interfacial bonding. Entropy engineering provides a promising route for such M-site design, because multiple transition metals can be distributed over the same crystallographic sublattice to introduce configurational complexity, local lattice distortion, and bonding heterogeneity. This concept has produced important progress in high-entropy carbides and other compositionally complex ceramics, where lattice distortion and chemical heterogeneity have been used to tailor hardness and mechanical response [14–18]. In MAX phases, recent studies have demonstrated that medium- and high-entropy M-site solid solutions can be synthesized while retaining the layered structure [19–23]. Beyond entropy-engineered systems, studies on V-doped Ti_2GaC have shown that M-site substitution can modify microstructure and mechanical properties [24], while first-principles calculations on M_2AlC-type carbides reveal composition-dependent elastic anisotropy and related physical properties [25]. Dynamic compression studies of highly oriented Ta_2AlC further indicate that microstructural orientation and confinement can strongly influence mechanical response [26]. These results collectively suggest that the mechanical behavior of MAX ceramics is sensitive not only to phase formation, but also to M-site chemistry, bonding environment, and microstructural state. However, configurational complexity alone does not necessarily lead to simultaneous improvements in strength and fracture toughness. For example, the reported medium-entropy $(Ti,V,Nb,Ta)_2AlC$ showed enhanced strength and hardness, whereas its fracture toughness was not improved relative to the corresponding reference MAX phase [19]. This distinction highlights the need to separate strengthening from toughening and to identify how individual M-site elements contribute to local bonding and fracture resistance. Nevertheless, systematic studies on Ta-based 211 MAX ceramics that compare different M-site medium-entropy combinations and relate the measured strength–toughness balance to element-resolved bonding remain limited.

A recent study on $Ti_3C_2T_x$-reinforced Ta_2AlC suggested that Ti can be incorporated into the M sublattice during high-temperature processing, and that limited Ti-related solid-solution formation may contribute to improved flexural strength and fracture toughness [27]. This observation provides an experimental clue and a practical starting point for extending M-site alloying in Ta_2AlC beyond minor Ti incorporation. In the present work, Ti, Nb, and V were selected as M-site alloying elements by considering both the prior Ti-solid-solution evidence and the carbide/nitride-forming character of these early transition metals. Compared with Ta, these elements also offer lower atomic masses and different atomic sizes, allowing the M-site chemistry to be modified while introducing local lattice distortion and bonding heterogeneity. Four Ta-based medium-entropy 211 MAX ceramics, namely $(TaNbV)_2AlC$, $(TaTiNb)_2AlC$, $(TaTiV)_2AlC$, and $(TaTiNbV)_2AlC$, were therefore designed to compare ternary and quaternary M-site combinations rather than simply maximize configurational entropy. The room-temperature flexural strength and fracture toughness were first evaluated experimentally and interpreted in relation to phase constitution, crystal structure, elemental distribution, and fracture morphology. Density functional theory (DFT) calculations combined with crystal orbital Hamilton population (COHP) analysis were then used to quantify element-resolved M–C and M–Al bonding, providing an atomistic basis for understanding the composition-dependent mechanical response. To extend this static bonding picture to finite-temperature behavior, a validated Deep Potential molecular dynamics (DP-MD) model was employed to examine structural retention, tensile softening, and basal-cleavage resistance under thermal loading. Finally, two mechanics-based bridging models were established to connect the room-temperature experimental properties with the DP-MD-derived tensile and cleavage descriptors, enabling prediction of high-temperature strength and toughness retention. The main contribution of this work is a systematic, element-resolved bonding analysis combined with a deep-potential-based finite-temperature bridging framework that links M-site chemistry to the strength–toughness balance and its elevated-temperature retention in Ta-based

medium-entropy 211 MAX ceramics, providing a basis for evaluating related MAX ceramics for high-temperature structural and protective applications.

2 Experimental and Computational Methods

2.1 Synthesis of MAX phases

Ta_2AlC was prepared as the reference ceramic, and four Ta-based medium-entropy 211 MAX ceramics were designed by equimolar occupation of the M sublattice, namely $(TaNbV)_2AlC$, $(TaTiNb)_2AlC$, $(TaTiV)_2AlC$, and $(TaTiNbV)_2AlC$. For clarity, $(TaNbV)_2AlC$, $(TaTiNb)_2AlC$, and $(TaTiV)_2AlC$ denote $(Ta_{1/3}Nb_{1/3}V_{1/3})_2AlC$, $(Ta_{1/3}Ti_{1/3}Nb_{1/3})_2AlC$, and $(Ta_{1/3}Ti_{1/3}V_{1/3})_2AlC$, respectively, while $(TaTiNbV)_2AlC$ denotes $(Ta_{1/4}Ti_{1/4}Nb_{1/4}V_{1/4})_2AlC$.

Tantalum powder (< 30 μm, ⩾99.5 wt.%, Kerun Nano New Materials Co., Ltd., China), titanium powder (< 45 μm,⩾99.5 wt.%, Jinzhou Institute of Metal Materials, China), niobium powder (< 30 μm, ⩾99.5 wt.%, Kerun Nano New Materials Co., Ltd., China), vanadium powder (< 30 μm, ⩾99.5 wt.%, Chengdu Huayin Powder Technology Co., Ltd., China), aluminum powder (< 29 μm,⩾99.7 wt.%, Harbin Northeast Light Alloy Powder Co., Ltd., China), and graphite powder (< 15 μm, ⩾99.0 wt.%, Qingdao Xingyuan Graphite Emulsion Co., Ltd., China) were used as raw materials. The starting powders were weighed according to a nominal molar ratio of M:Al:C = 2:1.2:0.95, where M represents Ta for the Ta_2AlC reference and the corresponding equimolar transition-metal mixture for the medium-entropy compositions. Excess Al was added to compensate for Al loss during high-temperature hot pressing. The nominal carbon content was set slightly below stoichiometry as part of the optimized starting-powder ratio for the present graphite-tooling vacuum hot-pressing route.

The weighed powders were loaded into polypropylene bottles together with zirconia balls at a ball-to-powder mass ratio of 1:1.5. The mixtures were homogenized in a horizontal mixer (model 5L2L, Yixing Dingshu Haoqiang Machinery Factory, China) at 100 r/min for 48 h. During mixing, the bottles were taken out every 4–6 h and manually shaken to reduce local powder accumulation and

agglomeration. After mixing, the powders were loaded into graphite dies equipped with graphite punches. The powder compacts were pre-pressed to 20 MPa within 5 min and held for 3 min to improve powder contact before reactive hot pressing.

All ceramics were fabricated by vacuum hot pressing in a ZT-40-21Y hot-pressing furnace (Shanghai Chenhua Technology Co., Ltd., China), with a furnace pressure of approximately 0.054 Pa. After pre-pressing, the die assembly was heated without external loading to 1350 °C. The pressure was then increased to 30 MPa at 1350 °C and maintained during the subsequent heating to 1500 °C and the 1 h holding stage. The heating rates were 10 °C/min from room temperature to 1200 °C, 6 °C/min from 1200 to 1350 °C, and 4.5 °C/min from 1350 to 1500 °C. After sintering, the samples were furnace cooled to room temperature and removed from the graphite dies, yielding disk-shaped bulk billets approximately 50 mm in diameter and ~3 mm in thickness. Photographs of the as-sintered billets are provided in **Fig. S1** in the **Electronic Supplementary Material (ESM)**. The billets were then machined or ground into specimens for subsequent characterization and mechanical testing.

2.2 Characterization and mechanical testing

The phase constitution of the sintered ceramics was examined by X-ray diffraction (XRD, D8 ADVANCE, Bruker, Germany) using Cu Kα radiation. The diffraction patterns were collected over a 2θ range of 10°–90° with a step size of 0.05° and a scanning rate of 1°/min. XRD was performed directly on the polished bulk surfaces of the hot-pressed specimens. To evaluate hot-pressing-induced texture, patterns were additionally collected on two mutually perpendicular surfaces of each specimen—one with its normal parallel to the hot-pressing axis and one perpendicular to it. Rietveld refinement was performed using the *GSAS-II* software package to determine the lattice parameters and theoretical densities [28]. The bulk densities of the sintered samples were measured by the Archimedes method using deionized water as the immersion medium, and the relative densities were calculated from the ratio of the measured bulk density to the Rietveld-derived theoretical density. The mechanically polished surfaces were briefly etched in the HNO_3/HCl/H_2O solution (1:1:1, v/v/v) for

5 s, immediately rinsed with deionized water, and dried before SEM observation. Grain morphology was then quantified from these polished and lightly etched cross-sectional SEM micrographs by marker-controlled watershed segmentation. Three fields were analysed for each composition, and the projected grain-section length, width, and aspect ratio were determined.

For transmission electron microscopy (TEM) observations, thin discs with a diameter of 3 mm were mechanically ground to approximately 30 μm, mounted on copper rings, and further thinned by ion milling using a Gatan 691 Precision Ion Polishing System (Gatan Inc., USA). TEM and selected-area electron diffraction (SAED) were performed using a JEM-2100F microscope (JEOL Ltd., Japan) operated at 200 kV. High-angle annular dark-field (HAADF) imaging and energy-dispersive X-ray spectroscopy (EDS) mapping were conducted in scanning transmission electron microscopy (STEM) mode using the same instrument to examine the local crystal structure and elemental distribution.

Room-temperature flexural strength was measured by three-point bending using a ZQ990LA mechanical testing machine (Dongguan Zhiqu Precision Instrument Co., Ltd., China) according to GB/T 6569-2006. Bar specimens with dimensions of 3 mm × 4 mm × >36 mm were tested with a support span of 30 mm and a crosshead speed of 0.5 mm/min. Room-temperature fracture toughness was evaluated by the single-edge notched beam (SENB) method using specimens with dimensions of 2 mm × 4 mm × 24 mm, a notch depth of approximately 2 mm, and a support span of 16 mm. All flexural and SENB specimens were machined from the hot-pressed billets with a fixed geometry that was identical for every composition. The flexural bars were cut with their longitudinal axes perpendicular to the hot-pressing direction and were loaded parallel to the hot-pressing direction. For the SENB specimens, the loading direction was perpendicular to the hot-pressing direction, and the notch was oriented such that crack propagation proceeded within the billet plane, i.e. perpendicular to the hot-pressing direction. The different loading orientations were dictated by the billet geometry: the ~3 mm billet thickness could accommodate the 3 mm dimension of the flexural bars in the loading direction, but not the 4 mm specimen height (h) used for the SENB tests; consequently, the SENB

specimens had to be machined with h lying within the billet plane. The specimens were ground to their final dimensions, and the through-thickness notch was subsequently introduced by wire electrical-discharge machining using a 0.18 mm molybdenum wire, giving a notch width of approximately 0.2 mm; the notches were tested in the as-machined condition without razor-blade sharpening or pre-cracking. The loading rate for SENB testing was 0.5 mm/min. The fracture toughness was calculated using the following equation [29]:

$$K_{IC}=\frac{3FL\sqrt{a}}{2bh^2}\left[1.93-3.07\left(\frac{a}{h}\right)+14.53\left(\frac{a}{h}\right)^2-25.07\left(\frac{a}{h}\right)^3+25.8\left(\frac{a}{h}\right)^4\right] \quad (1)$$

where F is the fracture load, L is the support span, a is the notch depth, and b and h are the specimen width and height, respectively. Five valid specimens were tested for each composition, and the average values and standard deviations were used for comparison. A SENB test was accepted as valid only when (i) fracture initiated from the machined notch, (ii) the load–displacement response remained essentially linear up to the fracture load, with no off-notch failure or spurious compliance, and (iii) the measured a/h fell within 0.45–0.55. Statistical significance among compositions was evaluated by one-way analysis of variance (ANOVA) followed by Tukey's honestly significant difference (HSD) post-hoc test, with a significance level of 0.05. All statistical analyses were performed using Python 3.11 with the SciPy and statsmodels packages.

After mechanical testing, fracture morphology and representative fracture-surface elemental distributions were examined using a field-emission scanning electron microscope (FE-SEM, Nova NanoSEM 450, FEI, USA) equipped with an energy-dispersive X-ray spectroscopy (EDS) detector.

2.3 First-principles calculations and bonding analysis

Special quasirandom structures (SQSs) [30] were constructed using the mcsqs module of the Alloy Theoretic Automated Toolkit (ATAT) to represent random M-site occupation in the medium-entropy 211 MAX phases [31]. The SQS models were built based on the primitive unit cell of 211-type Ta_2AlC. According to the crystallographic sublattices of the MAX structure, Ta, Ti, Nb, and V were allowed to occupy only the M sublattice, whereas Al and C were fixed on the A and X sublattices, respectively.

The M-site chemical disorder was represented using 96-atom SQS supercells. The selected SQS models showed zero or near-zero correlation deviations in the main coordination shells and were used as structural models for the subsequent first-principles calculations.

Density functional theory (DFT) calculations were performed using Quantum ESPRESSO [32,33]. The generalized gradient approximation with the Perdew–Burke–Ernzerhof (PBE) exchange-correlation functional [34] was used together with ultrasoft pseudopotentials. Dispersion interactions were considered using the DFT-D3 correction [35]. Structural optimization was carried out using variable-cell relaxation. Based on convergence tests using the quaternary $(TaTiNbV)_2AlC$ SQS model as the representative structure, a wavefunction cutoff energy of 50 Ry, a charge-density cutoff energy of 500 Ry, and a 3 × 4 × 3 k-point grid were adopted for the main SQS calculations. These settings were applied consistently to all investigated medium-entropy compositions. Gaussian smearing was used for the electronic occupations. The cutoff and k-point convergence tests are provided in **Fig. S2** in the **ESM**, and the DFT-optimized ternary SQS structures are shown in **Fig. S3** in the **ESM**. Optimized structures were visualized using *VESTA* [36].

Chemical bonding was evaluated by crystal orbital Hamilton population (COHP) analysis using the LOBSTER package [37–39], and the averaged negative integrated COHP value, denoted as −ICOHP, was used to compare the M–C and M–Al bonding.

2.4 Deep Potential model training and molecular dynamics simulations

A Deep Potential (DP) model [40] was trained for the Ta–Ti–Nb–V–Al–C chemical space using DeePMD-kit [41,42]. The element type map was set as Ta, Ti, Nb, V, Al, and C, and the se_e2_a DeepPot-SE descriptor [43] was adopted. Four independently initialized models were trained and used for model-deviation evaluation within the DP-GEN concurrent-learning workflow [44]. Configuration exploration was performed using LAMMPS [45] coupled with the DeepMD interface. The explored configurations included thermally perturbed bulk structures, tensile deformation configurations, cleavage configurations, and surface-slab configurations. The selected configurations were then

labeled by DFT using the same exchange-correlation functional, pseudopotentials, dispersion correction, and convergence criteria as described in **Section 2.3**. Detailed network architecture, training schedule, and loss prefactors are provided in **Section S3** of the **ESM**, and the representative training and validation curves are shown in **Fig. S4**.

Finite-temperature molecular dynamics simulations were performed using the trained DP model in LAMMPS. Bulk NPT simulations for the thermal-expansion analysis were performed at 300, 450, 600, 750, 900, 1050, 1200, 1350, and 1500 K, and the simulated XRD patterns and partial radial distribution functions were evaluated at 300, 1200, and 1500 K. The 96-atom SQS structures were used as parent cells for constructing larger periodic MD supercells. Supercell-size convergence of the z-direction tensile response was examined using the representative quaternary $(TaTiNbV)_2AlC$ model, as summarized in **Table S1**. The 2×2×3 supercell containing 1152 atoms was selected for the production DP-MD tensile and cleavage simulations as a balance between convergence and computational cost. In this MD supercell, the z direction corresponds to the basal-normal direction inherited from the layered 211 MAX structure. Tensile loading was therefore applied along z to probe the intrinsic resistance to layer-normal deformation, consistent with the strong anisotropy and basal-plane-related deformation characteristics of MAX phases [1,46,47]. Cleavage simulations were performed by opening sampled (0001) interfaces along the basal-normal direction, as {0001} basal-plane delamination has been identified as an important crack-wake bridging mechanism in the bulk fracture of MAX phases [48]. Additional surface-slab simulations were conducted at 900 and 1500 K to examine the behavior of free-surface configurations. Detailed simulation settings, including time steps, equilibration procedures, deformation and opening protocols, and ensemble parameters, are summarized in **Section S3** of the **ESM**.

The tensile and cleavage descriptors were extracted from the corresponding stress–strain and traction–separation curves. The ultimate tensile strength was defined as the maximum stress along the smoothed tensile stress–strain curve:

$$\sigma_{UTS}=\max[\sigma_z(\varepsilon_z)] \quad (2)$$

The tensile work density before instability was calculated as

$$U_t=\int_0^{\varepsilon_f}\sigma_z(\varepsilon_z)d\varepsilon_z \quad (3)$$

where ε_f denotes the strain associated with tensile instability. The tensile-strength retention was defined as

$$R_\sigma(T)=\sigma_{UTS}(T)/\sigma_{UTS}(300\text{K}) \quad (4)$$

For cleavage simulations, the traction–separation response was analyzed following the description commonly used in cohesive-zone and atomistic interface-separation analyses [49,50]. The peak cleavage traction was defined as

$$\sigma_c=\max[t_n(\Delta)] \quad (5)$$

where tn is the normal traction and Δ is the opening displacement. The work of separation, W_{sep}, was obtained from the positive area under the baseline-corrected traction–separation curve:

$$W_{sep}=\int_0^{\Delta_{end}}t_n(\Delta)d\Delta \quad (6)$$

where Δ_{end} denotes the final separation after interfacial detachment. Atomic structures and MD trajectories were visualized using OVITO [51].

3 Results and Discussion

3.1. Phase formation and structural characterization

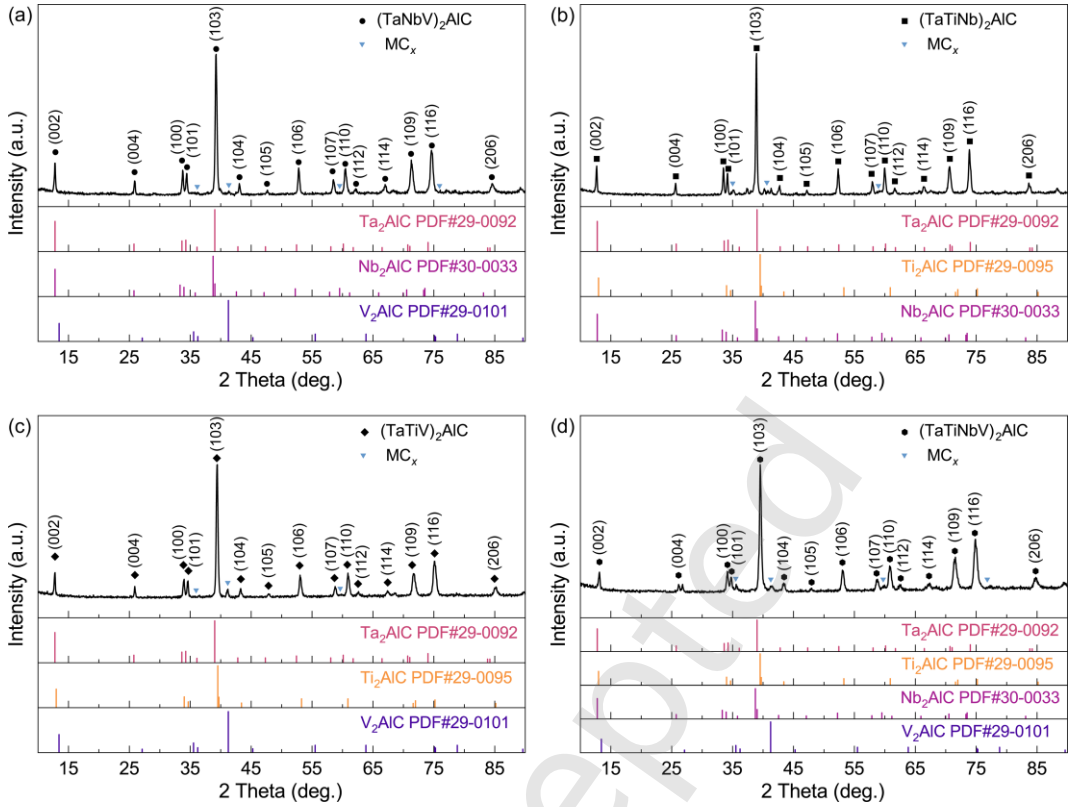

Fig. 1 XRD patterns of the synthesized Ta-based medium-entropy 211 MAX ceramics, with the secondary-phase (MC_x) reflections marked and the reference peak positions of related M_2AlC phases shown.

The nominal M-sublattice configurational entropies of the investigated compositions are summarized in **Table S2**. The phase constitution of the Ta-based medium-entropy MAX ceramics was first examined by XRD. As shown in **Fig. 1**, all four compositions are dominated by sharp diffraction peaks that can be indexed to the 211-type MAX phase structure. The low-angle basal reflections, such as (002) and (004), together with a series of non-basal reflections including (100), (101), (103), (104), (105), (106), (107), (110), (112), (114), (109), (116), and (206), are observed in the measured patterns. In all compositions, the strongest reflection is indexed as (103), which is a characteristic intense reflection of M_2AlC-type MAX phases. The measured peak positions are generally consistent with the reference patterns of related 211 MAX phases, including Ta_2AlC, Ti_2AlC, Nb_2AlC, and V_2AlC. Slight differences in peak positions among the four compositions suggest changes in the average lattice parameters caused by different M-site elemental combinations, rather than a change in the 211 MAX

structural framework. Very weak additional reflections, marked as MC_x in **Fig. 1**, are visible in some patterns and are attributed to a minor rock-salt-type secondary carbide; nevertheless, the overall diffraction response is clearly dominated by the 211-type MAX phase. These XRD results show that the layered M_2AlC-type framework was preserved after Ti, Nb, and/or V alloying under the present vacuum hot-pressing conditions.

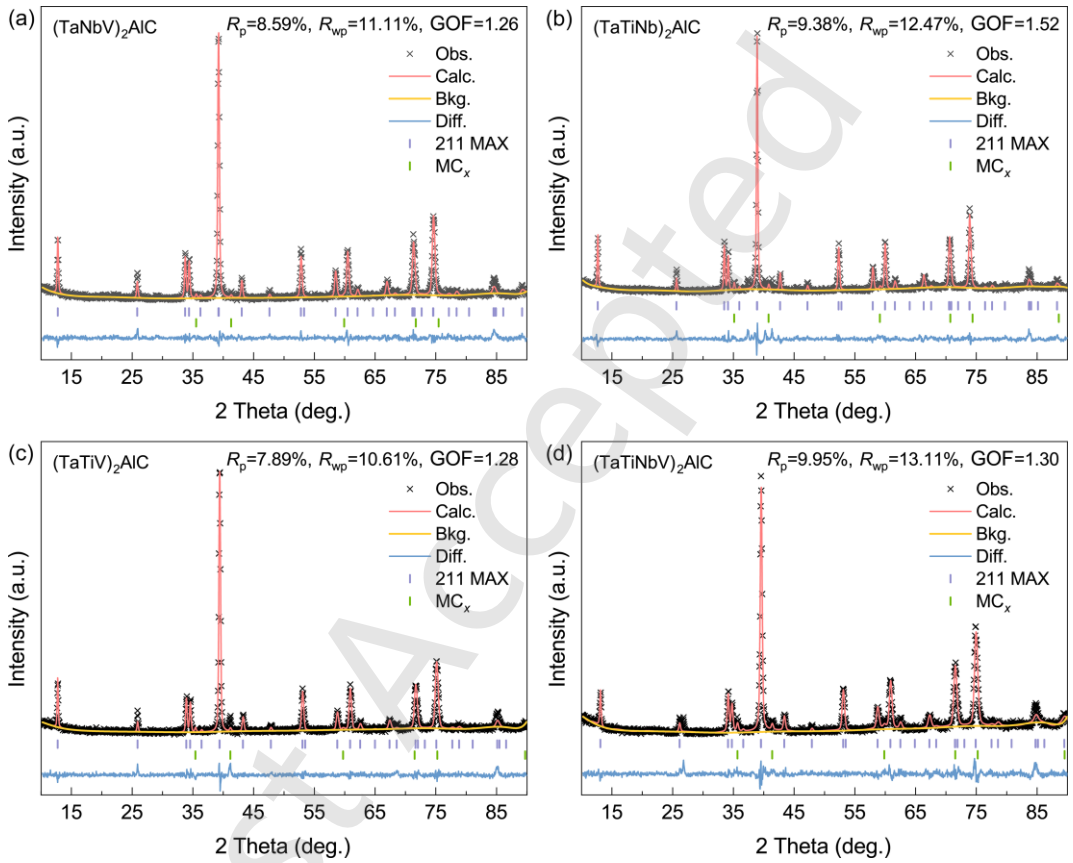

Fig. 2 Two-phase Rietveld refinements (211 MAX phase and minor rock-salt-type carbide) of the XRD patterns of Ta-based medium-entropy 211 MAX ceramics.

A two-phase Rietveld refinement, comprising the 211 MAX phase and a minor rock-salt-type secondary carbide (space group $Fm\bar{3}m$), was then performed to quantify the phase constitution and the 211 MAX crystallographic framework. As shown in **Fig. 2**, the calculated profiles reproduce the observed patterns for all four compositions, including the weak secondary-phase reflections, and the difference curves remain low over the measured 2θ range. The refined reliability factors are R_p = 7.89–9.95%, R_{wp} = 10.61–13.11%, and GOF = 1.26–1.52, within an acceptable range for two-phase

refinement of these Ta-based medium-entropy ceramics. The refinement confirms that all compositions are dominated by the 211 MAX phase (98.10–99.01 wt%), with only a minor rock-salt-type carbide (0.99–1.90 wt%). The refined 211 MAX lattice parameters vary systematically with the M-site combination, consistent with the peak shifts noted above, while the layered 211 framework is preserved in all cases. The 211 MAX texture index *J*, refined from XRD collected on the bulk surface whose normal is parallel to the hot-pressing axis, ranges from 1.48 to 2.43 among the medium-entropy compositions, indicating a composition-dependent preferred orientation. The full phase constitution, lattice parameters, secondary-phase contents, and texture indices for all compositions, including the Ta_2AlC reference, are summarized in **Table S3**. The XRD pattern and two-phase Rietveld refinement of the Ta_2AlC reference are provided in **Fig. S5**.

The local crystal structure and elemental distribution of the Ta-based medium-entropy MAX ceramics were further examined by TEM-based characterization. **Fig. 3** shows representative HAADF-STEM images, SAED patterns, and STEM-EDS elemental maps of $(TaNbV)_2AlC$, $(TaTiNb)_2AlC$, $(TaTiV)_2AlC$, and $(TaTiNbV)_2AlC$. The SAED patterns collected from the examined grains exhibit sharp and well-defined diffraction spots, indicating good crystallinity in the selected regions. For all four compositions, the patterns were recorded along the [0001] and $[11\bar{2}0]$ zone axes, and the reciprocal-lattice vector magnitudes ($|g|$, in nm^{-1}) and interspot angles are labelled directly in **Fig. 3**. In the [0001] patterns, the symmetry-equivalent $\{10\,\bar{1}\,0\}$-type reflections are separated by approximately 59–61°, consistent with the six-fold symmetry of the basal plane. In the $[11\bar{2}0]$ patterns, the (0002) and $(1\bar{1}00)$ reflections are mutually perpendicular (≈90°), and the measured $d(0002) \approx 0.69$ nm corresponds to $c \approx 1.37$–1.38 nm, in agreement with the XRD-refined lattice parameters. These diffraction features independently confirm the hexagonal layered structure of the 211 M_2AlC-type MAX phases [19,52]. The corresponding STEM-EDS maps show that the designed M-site elements are distributed throughout the examined regions. For each composition, Ta is co-distributed with the relevant alloying elements among Ti, Nb, and V within the observed grains, and no obvious Ti-, Nb-,

or V-rich segregated domains are observed at the spatial scale resolved by the present STEM-EDS measurements. The Al and C signals, where shown, are also associated with the same MAX-phase regions. Together with the XRD and Rietveld refinement results, the SAED and STEM-EDS results provide local structural and compositional evidence for the formation of crystalline Ta-based medium-entropy 211 MAX ceramics.

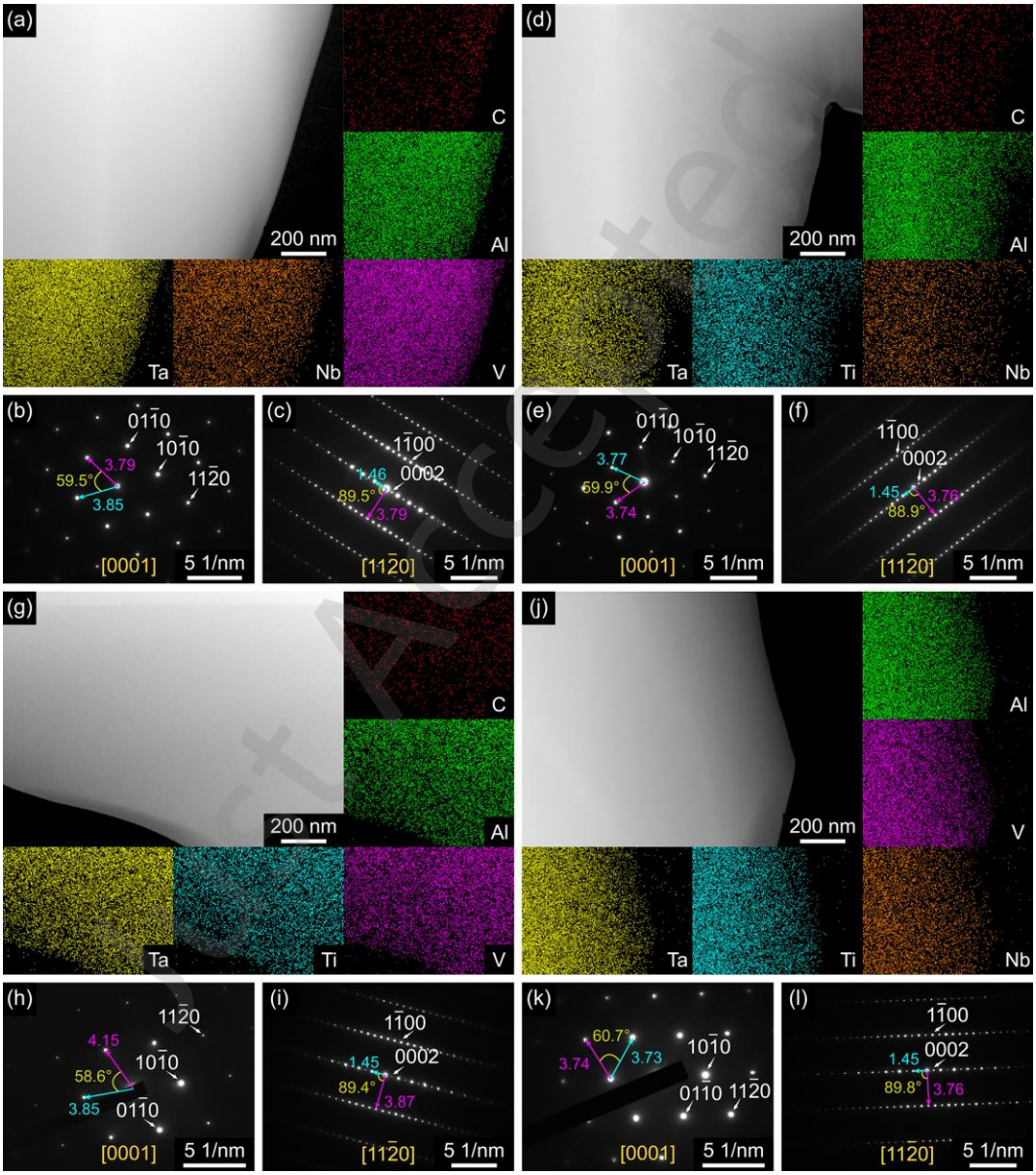

Fig. 3. Local crystal structure and elemental distribution of Ta-based medium-entropy 211 MAX ceramics. HAADF-STEM images, STEM-EDS elemental maps, and SAED patterns of (a–c) $(TaNbV)_2AlC$, (d–f) $(TaTiNb)_2AlC$, (g–i) $(TaTiV)_2AlC$, and (j–l) $(TaTiNbV)_2AlC$. The SAED

patterns were indexed along the [0001] and [11$\bar{2}$0] zone axes, with the reciprocal-lattice vector magnitudes (|*g*|, in nm^{-1}) and interspot angles labelled, and the elemental maps show the spatial distribution of the constituent elements in the observed regions.

As complementary characterization of the reference ceramic before the following density and mechanical-property comparison, the fracture surface and corresponding EDS maps of the hot-pressed Ta_2AlC reference are provided in **Fig. S6**.

3.2 Density and room-temperature mechanical properties

The density and room-temperature mechanical properties of the Ta-based medium-entropy 211 MAX ceramics are summarized in **Fig. 4**. As shown in **Fig. 4**a, the Rietveld-derived theoretical densities decrease from 7.6745 g·cm^{-3} for $(TaNbV)_2AlC$ to 6.7442 g·cm^{-3} for $(TaTiNbV)_2AlC$, while the corresponding Archimedes bulk densities decrease from 7.5372 to 6.6397 g·cm^{-3}. This density reduction reflects the partial replacement of the heavy Ta sublattice by lighter Ti, Nb, and V elements. The relative densities of all four medium-entropy ceramics remain high, ranging from approximately 98.13% to 98.59%, indicating that dense bulk ceramics were obtained under the present vacuum hot-pressing conditions.

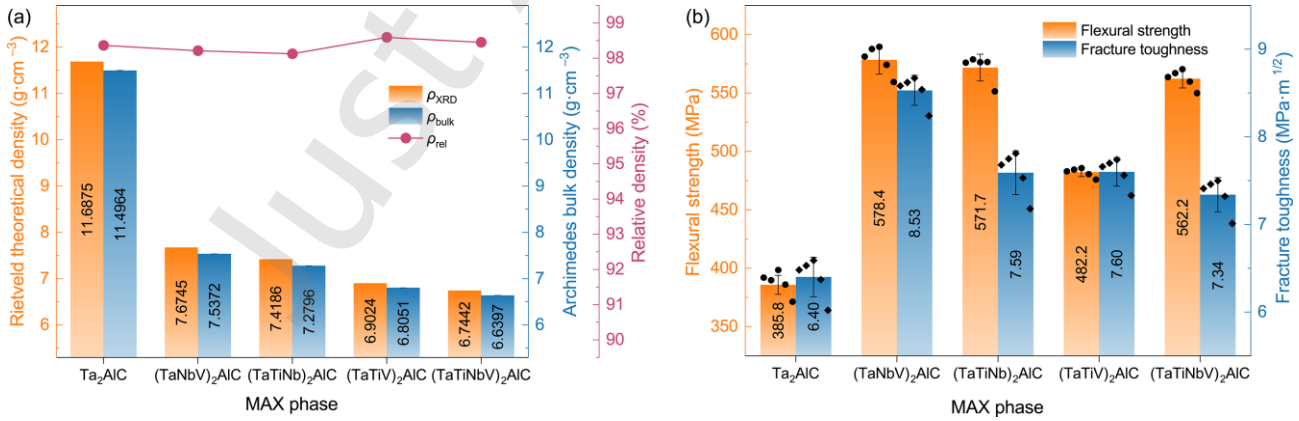

Fig. 4 Density and room-temperature mechanical properties of the Ta_2AlC reference and the four Ta-based medium-entropy 211 MAX ceramics: (a) Rietveld-derived theoretical density, Archimedes-measured bulk density, and relative density; (b) room-temperature flexural strength and fracture toughness of the Ta_2AlC reference and the medium-entropy ceramics. In (b), bars represent the mean

of five specimens and error bars denote ± one standard deviation; the overlaid symbols show the individual measurements of the five specimens (circles: flexural strength; diamonds: fracture toughness), horizontally offset for clarity, and the numbers on the bars are the mean values.

The room-temperature flexural strength and fracture toughness are compared in **Fig. 4**b. Representative room-temperature load–displacement curves are provided in **Fig. S7** of the **ESM**, while the individual crack-length ratios of the SENB specimens are listed in **Table S4**. The Ta_2AlC reference shows a flexural strength of 385.8 MPa and a fracture toughness of 6.40 $MPa \cdot m^{1/2}$. In comparison, all four medium-entropy ceramics exhibit simultaneous improvements in both properties, with flexural strengths of 482.2–578.4 MPa and fracture toughness values of 7.34–8.53 $MPa \cdot m^{1/2}$. Among them, $(TaNbV)_2AlC$ exhibits the best combined room-temperature mechanical response, with the highest flexural strength of 578.4 MPa and the highest fracture toughness of 8.53 $MPa \cdot m^{1/2}$, corresponding to increases of approximately 50% and 33% relative to Ta_2AlC, respectively. The other medium-entropy compositions also show higher strength and toughness than the Ta_2AlC reference, although their property levels vary with the specific M-site elemental combination; the statistical significance of these differences is assessed in **Section S6** and summarized in **Table S5**.

This coupled improvement differs from the previously reported equimolar Ti–V–Nb–Ta 211 MAX ceramic, in which strength and hardness were enhanced whereas fracture toughness showed no comparable improvement [19]. A similar distinction between hardening and toughening has also been reported in high-entropy carbide ceramics, where high hardness was achieved but fracture toughness remained limited in the absence of effective toughening mechanisms [53]. The contrast suggests that configurational complexity alone is insufficient to guarantee simultaneous strengthening and toughening in MAX ceramics. Instead, the mechanical response is more likely governed by the combined effects of element selection, densification, local bonding, microstructural features, and crack propagation within the layered 211 framework. Therefore, the present results establish the key experimental observation of this work: Ta-based medium-entropy alloying can reduce density while

improving the room-temperature strength–toughness balance, with $(TaNbV)_2AlC$ showing the most favorable combined performance among the investigated compositions.

The fracture-surface morphologies of the Ta-based medium-entropy 211 MAX ceramics are shown in **Fig. 5**. All four compositions exhibit relief-rich fracture surfaces composed of plate-like and lamellar grains. Parallel cleavage steps, layered terraces, and fractured lamellae are visible within individual grains, indicating that crack propagation mainly involves transgranular, cleavage-like lamellar cracking associated with the layered MAX structure [54,55]. Local separation between adjacent plate-like grains and abrupt changes in terrace orientation are also observed, suggesting the concurrent occurrence of intergranular separation and crack deflection. Therefore, the fracture behavior of these medium-entropy ceramics can be described as a mixed mode dominated by transgranular lamellar cracking, with local intergranular separation.

Although these fracture characteristics are broadly shared by all four compositions, several morphological differences can be observed. The fracture surface of $(TaNbV)_2AlC$ (**Fig. 5**a) is dominated by long and relatively well-preserved plate-like grains with continuous parallel cleavage steps. In contrast, $(TaTiNb)_2AlC$ (**Fig. 5**b) shows shorter and more fragmented lamellae, together with more visible gaps between adjacent plate-like grains. The $(TaTiV)_2AlC$ sample (**Fig. 5**c) displays pronounced interlayer delamination features and fractured lamellae with varied sizes. For the quaternary $(TaTiNbV)_2AlC$ sample (**Fig. 5**d), large lamellar grains intersect at multiple orientations, and dense layered terraces are observed. These representative images indicate that the fracture-surface morphology varies with the M-site elemental combination; however, because SEM fracture observations are local in nature, these morphological differences should be regarded as qualitative evidence rather than a direct quantitative explanation of the fracture-toughness ranking.

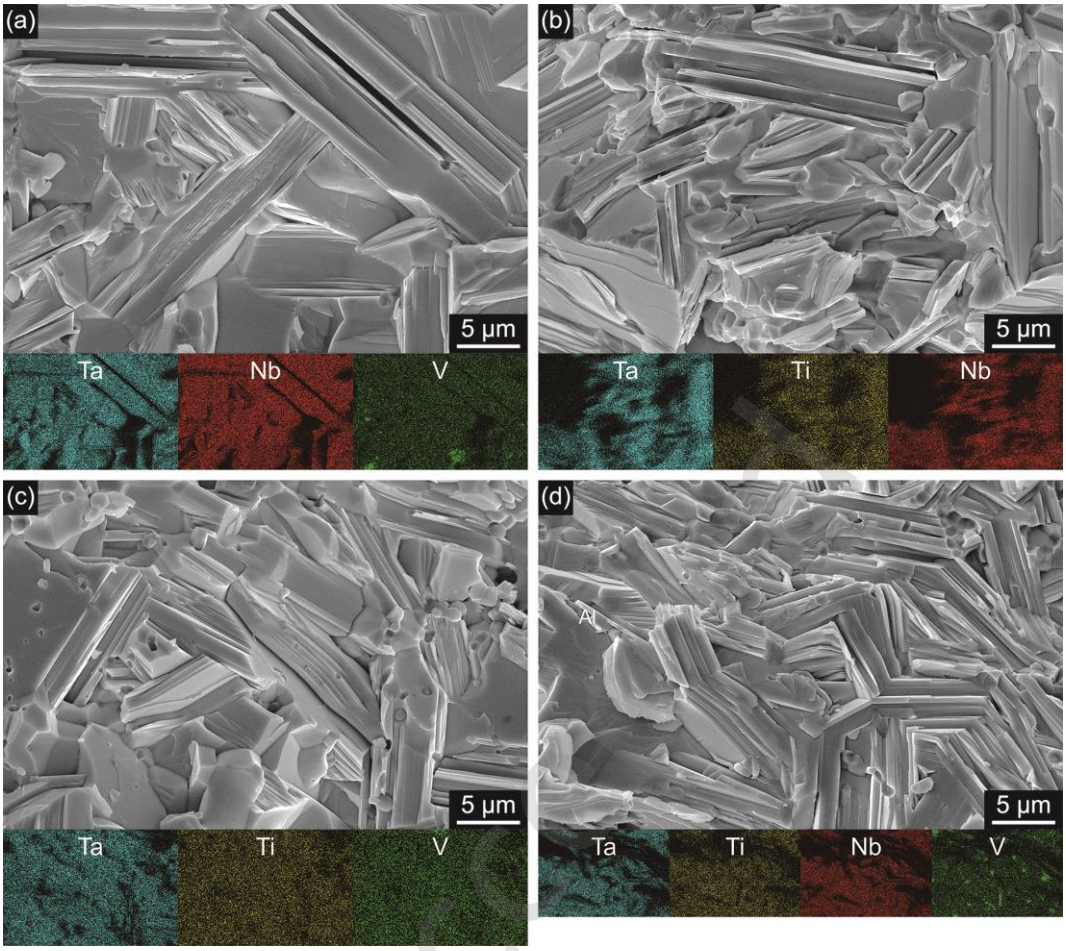

Fig. 5 Fracture-surface morphologies and EDS elemental maps of the Ta-based medium-entropy 211 MAX ceramics after room-temperature fracture testing: (a) $(TaNbV)_2AlC$, (b) $(TaTiNb)_2AlC$, (c) $(TaTiV)_2AlC$, and (d) $(TaTiNbV)_2AlC$.

Such terraced and lamellar fracture features are commonly reported in layered MAX ceramics, where anisotropic bonding and plate-like grain morphology can promote tortuous crack paths, interlayer delamination, grain bridging, and local grain pull-out [54,55]. In the present medium-entropy ceramics, the non-planar fracture surfaces, interrupted cleavage steps, and changes in lamellar orientation indicate that crack propagation does not proceed as simple flat cleavage, but involves crack-path deflection and local interlayer separation within the layered 211 framework. The EDS elemental maps collected from the fracture surfaces show that the designed M-site elements are distributed within the examined micrometre-scale regions, without obvious Ti-, Nb-, or V-rich segregated domains. Together with the XRD, Rietveld refinement, and TEM-based characterization results, the fracture-

surface EDS maps further support the formation of Ta-based medium-entropy 211 MAX ceramics with relatively homogeneous M-site elemental distribution at the spatial scale resolved by the present fracture-surface EDS measurements.

The polished-cross-section micrographs and corresponding grain-size statistics of all five compositions are provided in **Fig. S8** and **Table S6**. The projected grain-section dimensions and aspect ratios show substantially overlapping distributions across the five compositions; grain-size variation is therefore unlikely to be the primary cause of the observed composition-dependent differences in flexural strength and fracture toughness. Because hot pressing can induce crystallographic preferred orientation, the bulk texture of the ceramics was quantified by XRD on two mutually perpendicular bulk hot-pressed surfaces, whose normals were parallel (∥ HP) and perpendicular (⊥ HP) to the hot-pressing axis. The corresponding directional texture indices, J (∥ HP) and J (⊥ HP), and the (002)/(004) integrated-intensity ratios are listed in **Table S7**, and the two-direction XRD patterns are overlaid in **Fig. S9**. The texture is composition-dependent, ranging from the near-random Ta_2AlC reference J (∥ HP) = J (⊥ HP) ≈ 1.09 to the most strongly textured $(TaTiNbV)_2AlC$ J (∥ HP) ≈ 2.43 and J (⊥ HP) ≈ 2.80; the perpendicular-surface indices are semi-quantitative for the more strongly textured compositions. All specimens within each test type were machined and tested in a fixed orientation relative to the hot-pressing direction (**Section 2.2**); specifically, the flexural bars were machined with their longitudinal axes perpendicular to the hot-pressing direction and loaded parallel to it. Although the compositions exhibit a composition-dependent texture, its magnitude does not show a simple correspondence with the mechanical-property grouping: the most strongly textured $(TaTiNbV)_2AlC$ is neither the strongest nor the toughest composition, whereas the moderately textured $(TaNbV)_2AlC$ exhibits the highest flexural strength and fracture toughness. Because all specimens were tested in a fixed orientation relative to the hot-pressing direction, the comparison is not confounded by changes in testing geometry. These observations suggest that texture is unlikely to be the primary origin of the

observed composition-dependent property differences, although a contribution from bulk texture cannot be fully excluded.

3.3. Local structural distortion and element-resolved bonding

To clarify the atomic-scale structural and bonding effects of M-site medium-entropy alloying, DFT calculations and COHP analysis were performed using 96-atom SQS models. The optimized quaternary $(TaTiNbV)_2AlC$ SQS structure is shown as a representative model in **Fig. 6**a, while the optimized ternary SQS structures are provided in **Fig. S3**. The optimized lattice parameters and theoretical densities are also close to the Rietveld-refined values, indicating that the DFT-relaxed SQS models retain the average 211 MAX structural framework of the synthesized ceramics. After structural relaxation, the layered 211 MAX framework is retained, but local atomic displacements are visible around the chemically disordered M sublattice, reflecting the different atomic sizes and bonding characteristics of Ta, Ti, Nb, and V. The bond-length distortion, defined in this work as the standard deviation of the bond length divided by its mean (i.e. the coefficient of variation of the calculated bond lengths), is compared for M–C and M–Al bonds in **Fig. 6**b. The bond-length distortion is further found to be associated with the M-sublattice atomic-size mismatch, evaluated from the single-bond covalent radii of the constituent metals using the established multicomponent-alloy expression [56]: compositions with larger size mismatch generally show larger carbide-slab distortion, although this trend is not purely size-controlled and also reflects the element-specific bonding, as detailed in **Section S8** and **Table S8** of the **ESM**. For all four medium-entropy compositions, the M–C bonds show larger distortion than the M–Al bonds. The highest distortion is observed for $(TaNbV)_2AlC$, with δ_d values of 2.44% for M–C and 1.25% for M–Al, whereas $(TaTiNb)_2AlC$ exhibits the lowest distortion, with corresponding values of 1.05% and 0.49%. The $(TaTiV)_2AlC$ and $(TaTiNbV)_2AlC$ compositions show intermediate but still pronounced M–C distortion, both slightly above 2%. These results indicate that M-site alloying perturbs the carbide framework more strongly than the Al-containing interlayer environment. This behavior is consistent with the bonding anisotropy of MAX phases, where strong

M–X bonding within carbide/nitride slabs coexists with comparatively weaker M–A interactions between adjacent slabs [57,58].

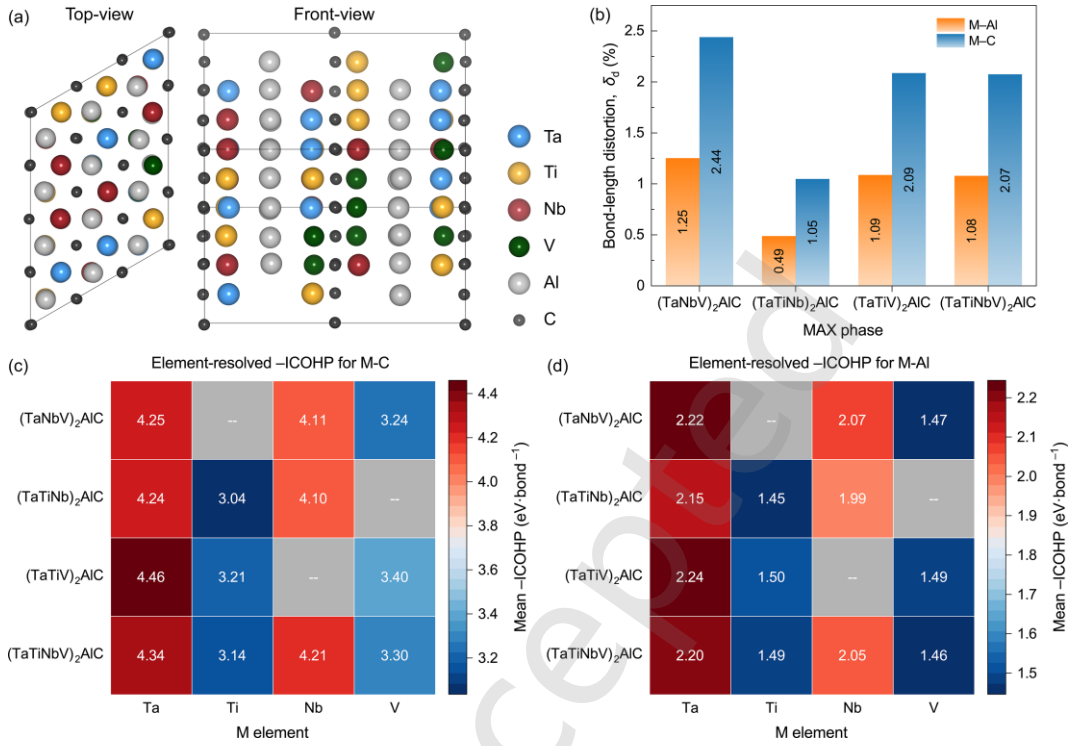

Fig. 6 Local structural distortion and element-resolved bonding in Ta-based medium-entropy 211 MAX ceramics: (a) representative DFT-optimized 96-atom SQS structure of $(TaTiNbV)_2AlC$; (b) bond-length distortion of M – C and M – Al bonds; (c,d) element-resolved mean –ICOHP values for M–C and M–Al bonds, respectively.

The element-resolved mean –ICOHP values reveal pronounced bonding heterogeneity within both the M–C and M–Al networks (**Fig. 6**c,d). For M–C bonds, Ta–C and Nb–C generally show larger mean –ICOHP values than Ti–C and V–C, indicating stronger local bonding contributions from Ta- and Nb-centered environments. In contrast, Ti–C and V–C exhibit lower values, although their exact magnitudes vary with composition. The M–Al bonds show a similar element-dependent tendency but with lower mean –ICOHP values overall, consistent with the weaker interlayer bonding character relative to M–C bonds. Thus, M-site medium-entropy alloying does not simply average the bonding features of the constituent elements; instead, it produces a chemically heterogeneous bonding network in which strong Ta/Nb-related bonds and relatively weaker Ti/V-related bonds coexist within the same

layered 211 framework. Representative raw M–C and M–Al bond-resolved –COHP curves for all four compositions are provided in **Fig. S10** and **Fig. S11**, respectively. The corresponding element-resolved M–C bond-length distributions are shown in **Fig. S12**.

A comparison among the four compositions shows that the bond-averaged –ICOHP trend is consistent with the grouping of the measured room-temperature flexural strength into statistically distinguishable levels (**Table S5**). The average M–C and M–Al bonding strengths are highest for $(TaNbV)_2AlC$ and $(TaTiNb)_2AlC$ and lowest for $(TaTiV)_2AlC$, consistent with the separation between the high-strength group of $(TaNbV)_2AlC$, $(TaTiNb)_2AlC$, and $(TaTiNbV)_2AlC$ and the lower-strength $(TaTiV)_2AlC$. The bonding analysis is therefore used to rationalize the separation between these strength groups rather than the small, statistically insignificant differences within the high-strength group. For brittle ceramics tested in bending, failure is commonly governed by crack initiation from tensile-side flaws under the maximum tensile stress; therefore, a stronger carbide framework can contribute to improved resistance against tensile-stress-driven crack initiation under flexural loading [59]. In this sense, the stronger Ta/Nb-related bonding provides a bond-level explanation for the higher flexural strength of $(TaNbV)_2AlC$ and $(TaTiNb)_2AlC$. The quaternary composition should not be interpreted as exhibiting an element-number-induced degradation: its room-temperature strength is statistically indistinguishable from that of $(TaNbV)_2AlC$, and its slightly lower bond-averaged −ICOHP values mainly reflect the reduced statistical fraction of the stronger Ta/Nb-centred bonds rather than enhanced lattice distortion or significant antibonding occupation. These composition-dependent trends further indicate that the configurational entropy itself is not the primary factor governing the strength–toughness balance in the present series. The three ternary compositions share an identical M-sublattice configurational entropy ($\Delta S_{mix}/R = \ln 3 = 1.10$; **Table S2**) yet separate into different strength groups, and the highest-entropy quaternary $(TaTiNbV)_2AlC$ ($\Delta S_{mix}/R = \ln 4 = 1.39$) exhibits neither the highest strength nor the highest toughness. The mechanical trends are therefore more consistently rationalized by the element-resolved bonding described above than by

configurational entropy alone, although elemental substitution and configurational entropy are intrinsically coupled in these compositions and cannot be fully separated. In contrast, the fracture-toughness ranking is not governed by the mean –ICOHP values alone. Although local bond strength is an important prerequisite for resisting bond rupture, fracture toughness describes crack-growth resistance and therefore depends on the crack-separation pathway, interlayer opening, crack deflection, grain morphology, porosity, and other microstructural factors. Therefore, the DFT calculations combined with COHP analysis mainly clarify the intrinsic bonding contribution to flexural strength, while the fracture resistance should be interpreted together with path-dependent cleavage descriptors and fracture-surface evidence.

3.4. Finite-temperature atomistic response from a validated Deep Potential model

To support finite-temperature atomistic simulations of the Ta-based medium-entropy 211 MAX ceramics, a Deep Potential model was trained for the Ta–Ti–Nb–V–Al–C chemical space and validated against DFT reference calculations. As shown in **Fig. 7**a and b, the DP-predicted relative energies and atomic forces agree well with the corresponding DFT values for the four medium-entropy compositions. The root-mean-square errors (RMSEs) for energy and force are 3.32 meV·atom^{-1} and 0.11 eV·Å^{-1}, respectively, providing an initial validation that the trained DP model reproduces the DFT potential-energy surface for the sampled configurations [40,60]. The equilibrium structural response was further examined using equation-of-state calculations. As shown in **Fig. 7**c, the DP energy–volume curves closely follow the corresponding DFT curves for all four compositions over the tested volume range. This agreement indicates that the model captures the volumetric energy response under compression and expansion, which is a key validation aspect for atomistic simulations involving thermal expansion and mechanical deformation [61]. In addition, the DP-optimized lattice parameters and densities are in close agreement with the DFT values, as summarized in **Table S9**, further confirming the accuracy of the DP model in reproducing the equilibrium structural properties of the investigated SQS models.

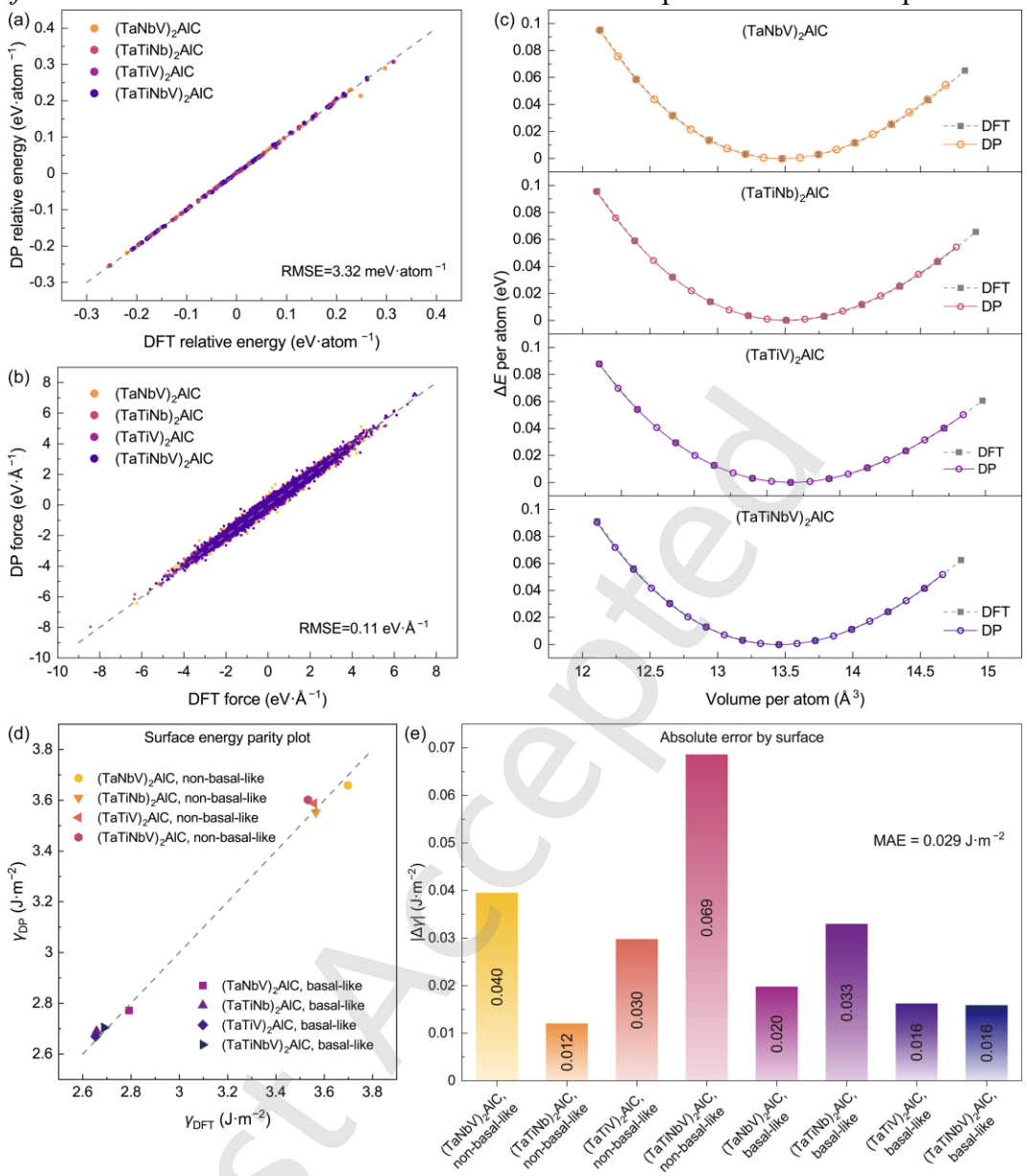

Fig. 7. Validation and surface-transferability assessment of the Deep Potential model for Ta-based medium-entropy 211 MAX ceramics: (a) parity plot of DP-predicted and DFT-calculated relative energies; (b) parity plot of DP-predicted and DFT-calculated atomic forces; (c) comparison of DP and DFT equation-of-state curves; (d) comparison of DP- and DFT-calculated surface energies for basal-like and non-basal-like slabs; and (e) absolute errors of DP-predicted surface energies relative to DFT values.

Besides bulk configurations, surface-containing configurations were also used to assess the model performance for bond-separation-related environments. This check is relevant because the subsequent

cleavage simulations involve the formation of free surfaces. The basal-like and non-basal-like surface slabs used for this comparison were not included in the training set. As shown in **Fig. 7**d and e, the DP-calculated surface energies agree well with the DFT values, with a mean absolute error of 0.029 $J \cdot m^{-2}$. The model also reproduces the higher surface energies of non-basal-like surfaces compared with basal-like surfaces, reflecting the anisotropic bonding nature of the layered MAX structure. These results support the use of the trained DP model for the comparative finite-temperature tensile and cleavage simulations conducted in this work [61,62].

To examine whether the trained Deep Potential model can describe the finite-temperature structural response of the Ta-based medium-entropy 211 MAX ceramics, DP-MD simulations were performed from 300 to 1500 K. As shown in **Fig. 8**a, the normalized volume of all four compositions increases smoothly with temperature, without an abrupt volume change over the simulated temperature range. The detailed temperature-dependent lattice parameters and volume changes are provided in **Fig. S13** and **Fig. S14**. This smooth expansion behavior indicates that the layered 211 framework is maintained during thermal equilibration within the present simulation time scale. The M–C partial radial distribution functions (RDFs) in **Fig. 8**b retain distinct nearest-neighbor and higher-shell peaks at 300, 1200, and 1500 K, indicating that the local M–C coordination is preserved during thermal equilibration [63]. The corresponding M–Al partial RDFs, which provide complementary information on the interlayer bonding environment, are shown in **Fig. S15**. With increasing temperature, the RDF peaks become broader and less intense, which is consistent with increased thermally induced atomic motion. The simulated XRD patterns in **Fig. 8**c also retain the main MAX-like diffraction features over the same temperature range, although peak broadening and intensity variations are observed at elevated temperature. Similar deep-potential MD studies have used finite-temperature structural and elastic responses to assess high-entropy ceramic systems [64,65]. Here, the RDF and MD-XRD results together suggest that the trained Deep Potential model preserves both local M–C coordination and average crystalline order during finite-temperature simulations within the present time scale.

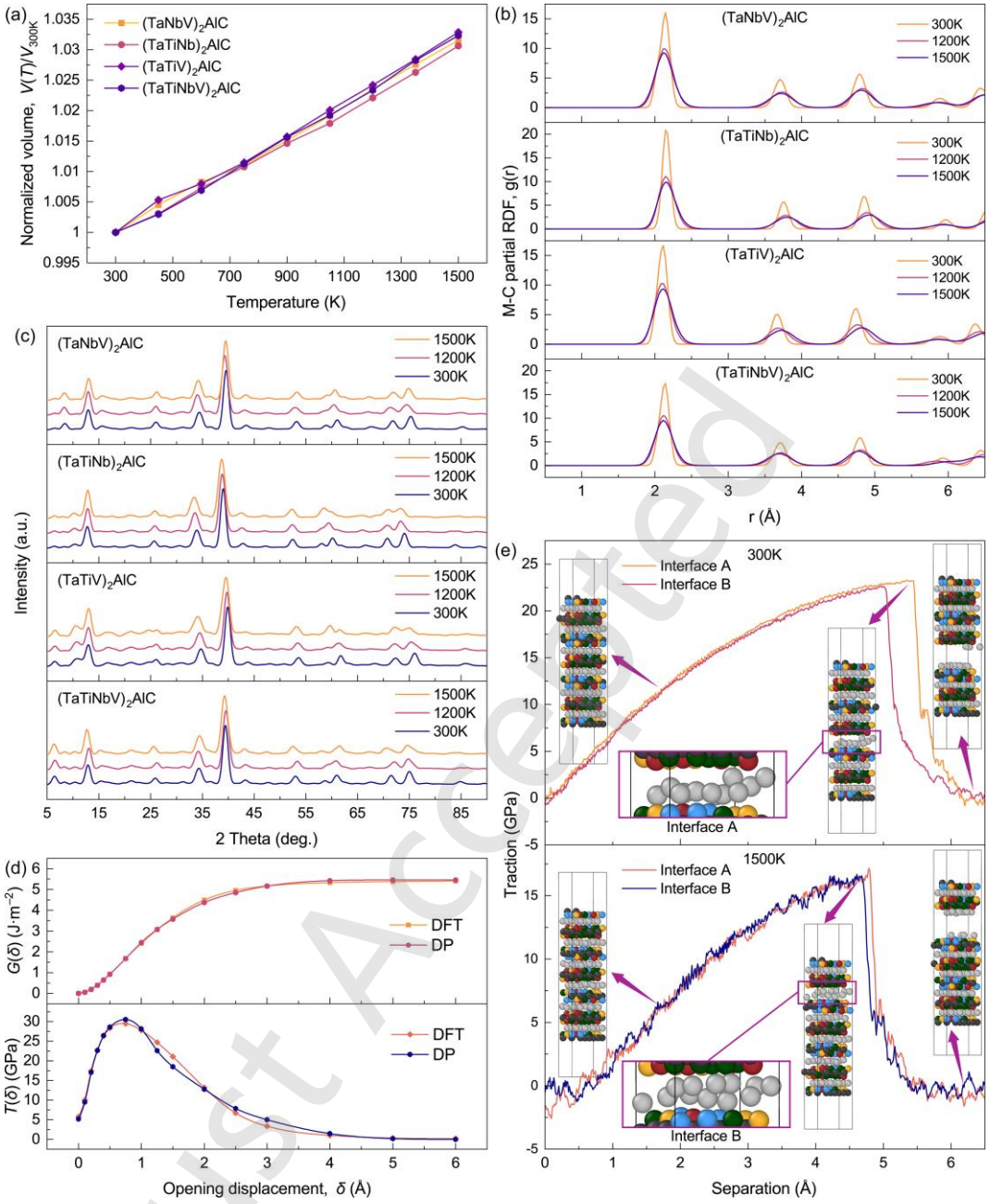

Fig. 8 Finite-temperature structural response and cleavage-path validation from DP-MD simulations: (a) normalized volume as a function of temperature; (b) M–C partial radial distribution functions at 300, 1200, and 1500 K; (c) simulated XRD patterns at different temperatures; (d) DP–DFT comparison of separation energy and traction for two representative (0001) cleavage interfaces in the quaternary (TaTiNbV)$_2$AlC model; and (e) finite-temperature traction–separation curves for the two representative (0001) cleavage interfaces in the quaternary (TaTiNbV)$_2$AlC model at 300 and 1500 K.

To further evaluate the model in fracture-relevant configurations, the DP-predicted separation-energy and traction profiles were compared with DFT results for two representative (0001) cleavage interfaces in the quaternary $(TaTiNbV)_2AlC$ model. This comparison extends the validation from near-equilibrium bulk configurations to large-separation configurations involving bond stretching, bond breaking, and free-surface formation, which are central to atomistic cleavage simulations [62,66]. As shown in **Fig. 8**d, the DP model reproduces both the magnitude and the relative difference of the DFT separation-energy and traction responses for the two interfaces. The finite-temperature traction–separation curves in **Fig. 8**e further show reduced peak traction and a broader separation response at 1500 K compared with 300 K, reflecting a thermally softened resistance to interface opening. These results support the use of the trained DP model for comparative finite-temperature tensile and cleavage simulations of the present Ta-based medium-entropy MAX ceramics.

After validating the finite-temperature structural response of the DP model, uniaxial tensile and cleavage simulations were performed using the size-converged 2×2×3 MD supercells constructed from the 96-atom SQS models (as shown in **Fig. 9**). The defect-free tensile simulations show clear thermal softening from 300 to 1500 K (**Fig. 9**a–d), and the corresponding full raw and smoothed stress–strain curves are provided in **Fig. S16**. This behavior is consistent with finite-temperature calculations on refractory ceramic systems, including transition-metal carbides, nitrides, and diborides, where elastic constants or moduli generally decrease with increasing temperature [67–70]. At 300 K, the compositions separate into a higher-strength group and lower-strength compositions in a way that is broadly consistent between the bond-averaged –ICOHP trend in **Fig. 6** and the room-temperature flexural-strength results in **Fig. 4**, suggesting that stronger average M–C/M–Al bonding contributes to the resistance against tensile-side crack initiation under bending. The bonding analysis is therefore used to rationalize the separation between the higher- and lower-strength groups rather than the small, statistically insignificant differences within the high-strength group (**Table S5**). Although the absolute tensile strengths are much higher than the measured flexural strengths, this difference is expected

because the simulations describe idealized defect-free atomistic deformation and do not include pores, surface damage, flaw populations, or specimen-scale stress statistics. At 1500 K, all four compositions retain approximately 78%–80% of their 300 K intrinsic tensile strengths. The pre-peak tensile work density decreases more markedly, from 3.01–3.30 GJ·m^{-3} at 300 K to 2.09–2.19 GJ·m^{-3} at 1500 K, indicating that elevated temperature reduces not only the peak tensile resistance but also the amount of tensile work accumulated before instability. Thus, **Fig. 9**a–d mainly serves to compare the composition-dependent retention of intrinsic tensile strength and pre-peak tensile work under the same finite-temperature loading protocol.

The cleavage simulations provide a complementary path-dependent descriptor of fracture-related separation response (**Fig. 9**e, f). At 300 K, the composition dependence of W_{sep} is broadly consistent with the measured room-temperature fracture-toughness trend in **Fig. 4**, with $(TaNbV)_2AlC$ showing the highest value and the quaternary composition giving a relatively low value among the medium-entropy ceramics. This trend is not captured as clearly by the static bond-averaged –ICOHP values in **Fig. 6**, because –ICOHP describes the bonding strength of relaxed equilibrium structures [71,72], whereas W_{sep} is obtained from the work required to progressively open a specific cleavage interface [49,50]. In other words, W_{sep} includes bond stretching, bond breaking, traction decay, and free-surface formation along the sampled separation path, which are more directly related to intrinsic resistance against cleavage [66]. Therefore, the relatively low 300 K W_{sep} of $(TaTiNbV)_2AlC$ suggests that increasing the number of M-site elements does not necessarily improve the path-dependent separation resistance, even when the average bonding strength remains high. At elevated temperature, the peak cleavage traction decreases for all compositions, whereas W_{sep} retention remains composition dependent. In particular, $(TaTiNbV)_2AlC$ retains a relatively high W_{sep} at 1500 K, indicating favorable predicted cleavage-work retention under the sampled separation path. This result should be interpreted as a finite-temperature atomistic projection rather than a direct high-temperature toughness measurement, because macroscopic fracture toughness also depends on microstructural crack-tip

shielding mechanisms such as crack deflection and grain bridging [73–75]. Overall, **Fig. 9** links the preceding bonding and mechanical results: bond-averaged –ICOHP and intrinsic tensile strength rationalize the flexural-strength trend, whereas path-dependent W_{sep} better reflects the intrinsic cleavage contribution to the fracture-toughness trend.

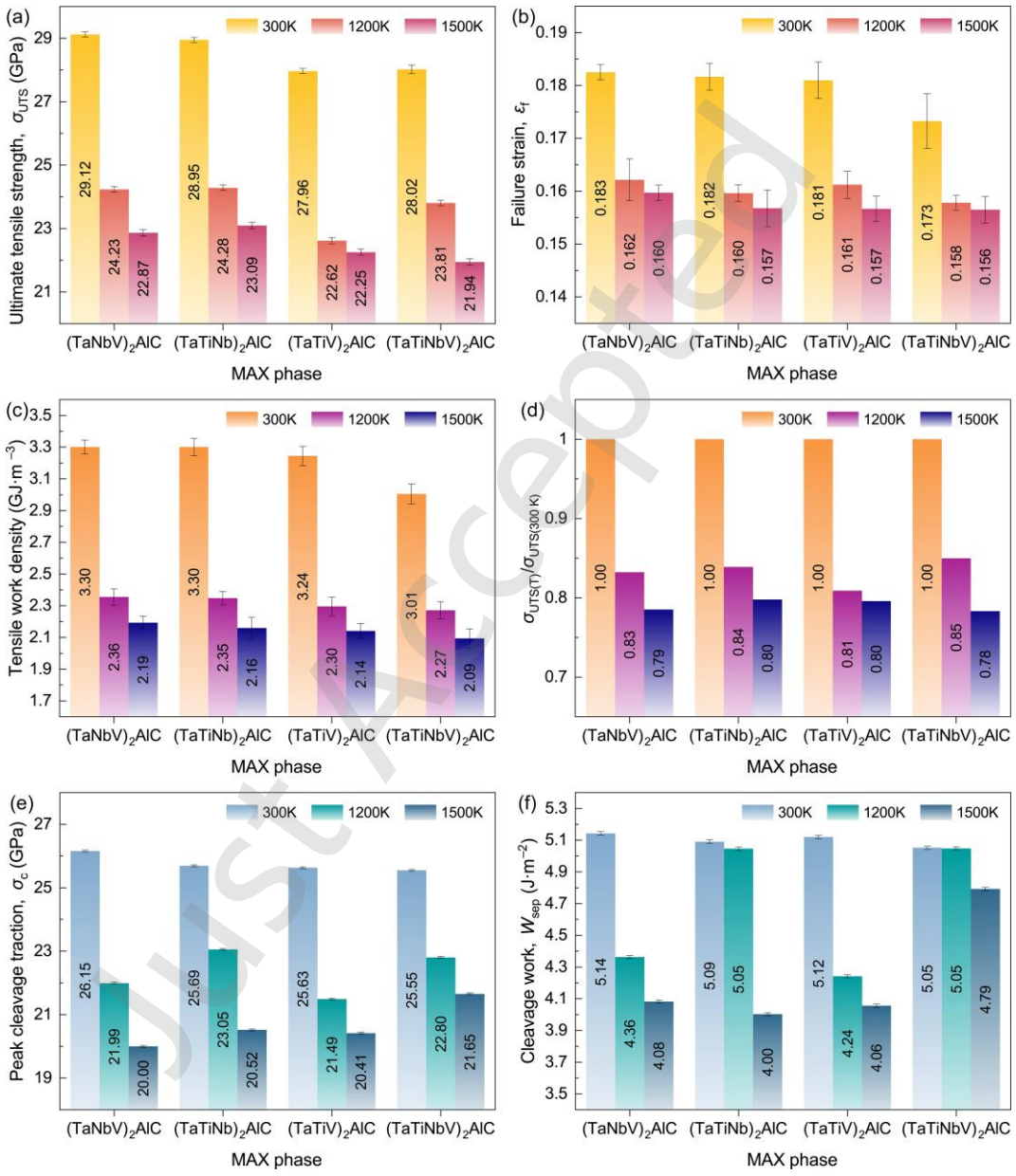

Fig. 9 Finite-temperature tensile softening and cleavage-work retention of Ta-based medium-entropy 211 MAX ceramics predicted by DP-MD simulations: (a) ultimate tensile strength, (b) failure strain, (c) pre-peak tensile work density, (d) tensile-strength retention, (e) peak cleavage traction, and (f) work of separation, W_{sep}, at 300, 1200, and 1500 K.

3.5. Experiment–DP-MD bridging projection of high-temperature strength and toughness

The fracture morphologies in **Fig. 5** show cleavage-like transgranular fracture, crack deflection, and layer-related separation features, indicating that the mechanical response of these layered MAX ceramics is controlled by both intrinsic bond separation and extrinsic specimen-scale effects. To connect the room-temperature experimental properties with the finite-temperature DP-MD descriptors, two bridging models were developed for flexural strength and fracture toughness, respectively. In both models, the measured 300 K properties provide the macroscopic reference state, while the temperature-dependent retention is determined from the DP-MD tensile and basal-cleavage responses. The detailed derivations are provided in the **ESM**. Both models are intended as qualitative-to-semiquantitative, first-order projections: the measured 300 K properties serve as composition-specific anchors, and the room-temperature defect-reduction and bridging factors are assumed to remain approximately unchanged over the short-time finite-temperature projection, so the resulting high-temperature values should be read as directional, order-of-magnitude estimates rather than absolute predictions.

For flexural strength, an energy-equivalent tensile-damage-controlled bending model was constructed from the DP-MD tensile modulus, ultimate tensile strength, strain at maximum stress, and pre-peak tensile work density. The tensile side of the beam was described by a DP-informed damage law, whereas the compressive side was treated as an elastic load-bearing region; neutral-axis migration was determined from axial force equilibrium. The predicted flexural strength was expressed as

$$\sigma_{\mathrm{b}}^{\mathrm{pred}}(p,T)=\sigma_{\mathrm{b}}^{\mathrm{exp}}(p,300\ \mathrm{K})R_{\mathrm{b}}^{\mathrm{DP}}(p,\mathrm{T}) \tag{7}$$

where p denotes the composition, T is the temperature, and $R_{\mathrm{b}}^{\mathrm{DP}}$ is the DP-derived flexural-strength retention factor. The detailed derivation of $R_{\mathrm{b}}^{\mathrm{DP}}$, including the energy-equivalent tensile damage function and neutral-axis-shifted bending integral, is provided in the **ESM**. **Fig. 10**a shows that the predicted high-temperature flexural strength is controlled by two factors: the room-temperature experimental anchor and the DP-derived intrinsic strength retention. The Ta–Nb–V-containing composition, $(TaNbV)_2AlC$, shows the highest room-temperature flexural strength and is predicted to

remain the strongest composition at 1500 K, consistent with the stronger Ta/Nb-related bonding contribution indicated by **Fig. 6** and the high intrinsic tensile strength in **Fig. 9**. Replacing Nb with Ti, as in $(TaTiV)_2AlC$, leads to the lowest absolute strength over the whole temperature range. This does not originate from an exceptionally rapid DP-predicted thermal degradation, but mainly from its lower room-temperature experimental anchor, implying a stronger macroscopic reduction from the intrinsic tensile response to the measured flexural strength. In contrast, $(TaTiNbV)_2AlC$ shows the highest projected macroscopic flexural-strength retention in **Fig. 10**a, although its advantage over $(TaTiV)_2AlC$ is marginal (approximately 77.1% versus 76.9%). This result applies specifically to the room-temperature-anchored bridging projection and should not be interpreted as evidence for a monotonic improvement in intrinsic tensile-strength retention with increasing M-site chemical complexity; in the DP-MD intrinsic tensile response (**Fig. 9**d) all four compositions retain approximately 78–80% and $(TaTiNbV)_2AlC$ is not the highest.

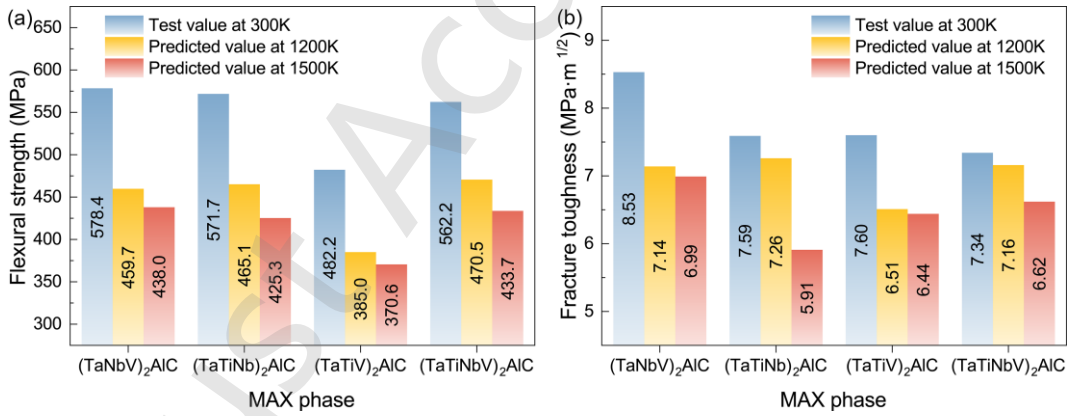

Fig. 10 Mechanics-based experiment–DP-MD bridging projections of high-temperature mechanical properties, presented as qualitative-to-semiquantitative first-order estimates: (a) flexural strength and (b) fracture toughness of Ta-based medium-entropy 211 MAX ceramics.

For fracture toughness, the DP-MD basal-cleavage response was incorporated through an energy-based fracture relation. In linear elastic fracture mechanics, the stress-intensity factor is related to the elastic modulus and fracture resistance through $K \sim (EG)^{1/2}$ [76]. Using the work of separation defined

in **Section 2.4** as the DP-MD descriptor of path-specific basal-cleavage resistance, a room-temperature-anchored toughness bridge was formulated as

$$K_{IC}^{pred}(p,T)=K_{IC}^{exp}(p,300\ \mathrm{K})\sqrt{\frac{E_{MD}(p,T)W_{sep}^{DP}(p,T)}{E_{MD}(p,300\ \mathrm{K})W_{sep}^{DP}(p,300\ \mathrm{K})}} \quad (8)$$

where p denotes the composition, T is the temperature, and E_{MD} is the DP-MD tensile modulus. The equation calibrates each composition to its measured 300 K fracture toughness and attributes the finite-temperature toughness retention to the DP-MD-predicted change in the product $E_{MD}W_{sep}^{DP}$. The detailed derivation, including the composition-specific net bridging factor, is provided in the **ESM**. This relation is an isotropic, Irwin-type first-order approximation: the effective crack-tip modulus is taken as the basal-normal DP-MD tensile modulus, i.e. the stiffness conjugate to the simulated (0001) basal-cleavage opening, and the small universal anisotropy index [77] (A^U = 0.06–0.13, **Table S10**) confirms that these phases are only weakly anisotropic, so the isotropic form is adequate at this first-order level. **Fig. 10**b reveals a different composition dependence from that of flexural strength. $(TaNbV)_2AlC$ has the highest absolute fracture toughness at room temperature and is predicted to retain the highest value at 1500 K, indicating that the Ta–Nb–V combination provides the most favorable balance between the measured macroscopic toughness and the DP-derived cleavage resistance. However, the quaternary $(TaTiNbV)_2AlC$ exhibits the highest toughness retention at elevated temperature. This trend originates from its relatively high W_{sep}^{DP} at 1500 K in **Fig. 9**f, showing that the broad M-site bonding distribution is beneficial for maintaining path-dependent cleavage resistance even though it does not give the highest room-temperature toughness. By contrast, $(TaTiNb)_2AlC$ maintains high predicted flexural strength at 1200 K but shows a pronounced decrease in fracture toughness at 1500 K, indicating that tensile-strength retention and cleavage-work retention are not governed by the same composition descriptor. Overall, Ta–Nb–V favors high absolute strength and toughness, Ti-containing quaternary alloying favors high-temperature retention, and the Ti–V combination without Nb gives the least favorable strength level in the present set of compositions.

A single-composition experimental consistency check for $(TaTiNb)_2AlC$ at 1250 °C in argon shows that the measured high-temperature flexural strength and fracture toughness agree with the bridging-model projections to within ~12–18% (**Section S12.3 and Fig. S17 of the ESM**), supporting the projected order of magnitude for this composition while indicating a systematic overestimation. It should be emphasized that the present DP-MD simulations and bridging-model projections describe the intrinsic, oxygen-free high-temperature behavior of these ceramics: because the Deep Potential does not include oxygen, all finite-temperature structural- and mechanical-retention results correspond to inert (argon/vacuum) conditions and do not capture oxidation. Under actual oxidative service environments, the high-temperature performance of MAX phases can additionally be governed by oxidation-related processes such as protective-scale formation, internal oxidation, and oxidation-assisted damage. A systematic experimental study of the composition-dependent oxidation behavior and its coupling with the mechanical response would be a valuable direction for future work.

4 Conclusions

In this work, four Ta-based medium-entropy 211 MAX ceramics, $(TaNbV)_2AlC$, $(TaTiNb)_2AlC$, $(TaTiV)_2AlC$, and $(TaTiNbV)_2AlC$, were synthesized and investigated through experimental characterization, DFT-based bonding analysis, DP-MD simulations, and mechanics-based bridging models. The main conclusions are summarized as follows.

(1) Dense Ta-based medium-entropy 211 MAX ceramics were successfully fabricated while retaining the layered M_2AlC-type framework. The incorporation of Ti, Nb, and V reduced the density compared with Ta-rich chemistry, while high relative densities of approximately 98.13%–98.59% were maintained. All four medium-entropy ceramics exhibited higher room-temperature flexural strength and fracture toughness than the Ta_2AlC reference. Among them, $(TaNbV)_2AlC$ showed the best combined room-temperature mechanical response, with a flexural strength of 578.4 MPa and a fracture toughness of 8.53 $MPa \cdot m^{1/2}$.

(2) DFT calculations combined with COHP analysis revealed pronounced element-resolved bonding heterogeneity in the M–C and M–Al networks. Ta- and Nb-centered environments generally provided stronger bonding contributions than Ti- and V-centered environments. The bond-averaged –ICOHP trend was consistent with the grouping of room-temperature flexural-strength into statistically distinguishable levels, indicating that strong Ta/Nb-related bonding enhances resistance to tensile-side crack initiation under bending. In contrast, fracture toughness was not controlled by average bond strength alone, because crack propagation in layered MAX ceramics also involves path-dependent separation and microstructural crack-deflection processes.

(3) The validated DP model reproduced the DFT energy, force, equation-of-state, and surface-energy responses, supporting its use for finite-temperature atomistic simulations. DP-MD results showed that the layered structural framework and local M–C coordination were retained from 300 to 1500 K under inert (oxygen-free) conditions within the present simulation time scale, as the Deep Potential does not include oxygen. The tensile simulations revealed thermal softening of intrinsic atomistic strength, whereas the cleavage simulations showed composition-dependent work-of-separation retention. In particular, $(TaTiNbV)_2AlC$ exhibited relatively high elevated-temperature W_{sep} retention, indicating that quaternary M-site chemical complexity can help maintain path-dependent cleavage resistance even though it does not maximize room-temperature toughness.

(4) Mechanics-based bridging models were established to connect the measured 300 K mechanical properties with DP-MD tensile and basal-cleavage descriptors. The projections indicate that $(TaNbV)_2AlC$ provides the highest absolute strength and toughness among the investigated medium-entropy compositions, whereas $(TaTiNbV)_2AlC$ exhibits the most favorable predicted high-temperature retention. The Ti–V-containing ternary composition without Nb, $(TaTiV)_2AlC$, shows the least favorable strength level, mainly because of its lower room-temperature experimental strength anchor. These results indicate that M-site medium-entropy alloying in Ta-based 211 MAX ceramics

should be designed by element-specific bonding and path-dependent fracture resistance, rather than by configurational entropy alone.

These results point to a composition-design principle for Ta-based 211 MAX ceramics: Ta/Nb-rich M–C and M–Al bonding networks are closely associated with high absolute strength and fracture toughness, whereas broader M-site chemical complexity is more favorable for retaining basal-cleavage resistance at elevated temperatures. Accordingly, optimizing Ta-based 211 MAX ceramics requires separately targeting the strong-bond network for mechanical performance and the basal-separation pathway for high-temperature fracture-resistance retention, rather than increasing M-site elemental diversity alone. These findings provide a mechanistic framework for entropy-engineered MAX ceramics in which room-temperature mechanical performance and elevated-temperature property retention are treated as related but distinct design objectives.

Acknowledgements

The authors thank Yue He, Chenrui Qian, and Shijie Pan from Hohai University for their assistance during the investigation and for many stimulating discussions. The authors also thank Junjing Ding from SCIXAS Lab (www.scixas.com) for ion-milled TEM specimen preparation and related characterization. The authors also gratefully acknowledge Bangjun Li from Southeast University for his assistance with the elevated-temperature mechanical property measurements.

During the preparation of this manuscript, DeepSeek was used only for language polishing and readability improvement. All authors reviewed, edited, and approved the final manuscript and take full responsibility for its scientific content.

Funding

This work was supported by the Science Foundation of the National Key Laboratory of Science and Technology on Advanced Composites in Special Environments, the Natural Science Foundation of

Jiangsu Province for Youths (BK20230948), and the National Natural Science Foundation of China (No. 52472090).

Author contributions

Lu Liu: Methodology, Software, Investigation, Formal analysis, Writing-Original Draft, Visualization, Funding acquisition. **Qifeng Zhuang:** Methodology, Data Curation, Formal analysis, Visualization. **Xiyu Xiao:** Methodology, Data Curation, Visualization. **Wei Ding:** Methodology, Data Curation. **Haoran Zhou:** Methodology, Data Curation. **Xuefang Yin:** Methodology, Investigation. **Kaicheng Zhang:** Investigation, Validation. **Baoze Zhao:** Investigation, Validation. **Shun Dong:** Writing-review & editing, Supervision. **Guobing Ying:** Conceptualization, Funding acquisition, Supervision.

Availability of data and materials

The data that support the findings of this study are available from the corresponding author upon reasonable request.

Competing interests

The authors have no competing interests to declare that are relevant to the content of this article.

Electronic Supplementary Material (ESM)

Electronic Supplementary Material, including specimen photographs; DFT convergence tests and optimized SQS structures; DP model training and supercell-size-convergence details; supplementary characterization of the Ta_2AlC reference and phase-constitution data for all compositions; room-temperature mechanical-testing details and statistical analyses; grain-size and two-direction texture analyses; COHP, bond-length, structural, and elastic-property data; additional finite-temperature

structural and tensile results; and derivations and experimental consistency checks of the mechanics-based bridging models, is available in the online version of this article.

References

[1]Barsoum MW, Radovic M. Elastic and Mechanical Properties of the MAX Phases. *Annu Rev Mater Res* 2011, **41**: 195–227.

[2]Rathod HJ, Ouisse T, Radovic M, *et al.* Room temperature crack-healing in an atomically layered ternary carbide. *Sci Adv* 2021, **7**: eabg2549.

[3]Zhang Z, Duan X, Jia D, *et al.* On the formation mechanisms and properties of MAX phases: A review. *J Eur Ceram Soc* 2021, **41**: 3851–78.

[4]Dahlqvist M, Barsoum MW, Rosen J. MAX phases – Past, present, and future. *Mater Today* 2024, **72**: 1–24.

[5]Xu Q, Zhou Y, Zhang H, *et al.* Theoretical prediction, synthesis, and crystal structure determination of new MAX phase compound V_2SnC. *J Adv Ceram* 2020, **9**: 481–92.

[6]Zhao S, Chen L, Xiao H, *et al.* Phase transformation and amorphization resistance in high-entropy MAX phase M_2SnC (*M* = Ti, V, Nb, Zr, Hf) under *in-situ* ion irradiation. *Acta Mater* 2022, **238**: 118222.

[7]Zhang GL, Du YQ, Hu MH, *et al.* Spark Plasma Sintering of Nove MAX Phase Mo_2Ga_2C. *Advanced Ceramics* 2023, **44**: 481–9.

[8]Griseri M, Tunca B, Lapauw T, *et al.* Synthesis, properties and thermal decomposition of the Ta_4AlC_3 MAX phase. *J Eur Ceram Soc* 2019, **39**: 2973–81.

[9]Sauceda D, Singh P, Falkowski AR, *et al.* High-throughput reaction engineering to assess the oxidation stability of MAX phases. *Npj Comput Mater* 2021, **7**: 6.

[10] Ma G, Zhang A, Wang Z, *et al.* MAX phase coatings: synthesis, protective performance, and functional characteristics. *Mater Horiz* 2025, **12**: 1689–710.

[11] Li X, Xie X, Gonzalez-Julian J, *et al.* Oxidation and creep behavior of textured Ti_2AlC and Ti_3AlC_2. *J Eur Ceram Soc* 2022, **42**: 364–75.

[12] Wyatt BC, Nemani SK, Hilmas GE, *et al.* Ultra-high temperature ceramics for extreme environments. *Nat Rev Mater* 2024, **9**: 773–89.

[13] Hu C, He L, Zhang J, *et al.* Microstructure and properties of bulk Ta_2AlC ceramic synthesized by an *in situ* reaction/hot pressing method. *J Eur Ceram Soc* 2008, **28**: 1679–85.

[14] Sarker P, Harrington T, Toher C, *et al.* High-entropy high-hardness metal carbides discovered by entropy descriptors. *Nat Commun* 2018, **9**: 4980.

[15] Xiang H, Xing Y, Dai F zhi, *et al.* High-entropy ceramics: Present status, challenges, and a look forward. *J Adv Ceram* 2021, **10**: 385–441.

[16] Liu Y, Zhu Z, Tang Z, *et al.* Unraveling Lattice-Distortion Hardening Mechanisms in High-Entropy Carbides. *Small* 2024, **20**: 2403159.

[17] Guo LW, Liu JX, Qin Y, *et al.* The Indentation Load Effect of Hardness of Non-Stoichiometric High-Entropy Carbides $(Ti_{0.2}Zr_{0.2}Hf_{0.2}Nb_{0.2}Ta_{0.2})C_{1-x}$. *Advanced Ceramics* 2024, **45**: 169–76.

[18] Mao M, Huo S, Chen L, *et al.* A new route to fabricate dual-phase compositionally complex ceramics. *J Eur Ceram Soc* 2024, **44**: 116726.

[19] Ma K, Shi X, He G, *et al.* In situ reaction synthesis, microstructure and thermomechanical properties of novel medium-entropy $(Ti,V,Nb,Ta)_2AlC$ ceramics. *Ceram Int* 2023, **49**: 21206–12.

[20] Cao L, Zhang Q, Du L, *et al.* Synthesis and characterization of high entropy $(TiVNbTaM)_2AlC$ (M = Zr, Hf) ceramics. *J Adv Ceram* 2024, **13**: 237–46.

[21] Cao L, Zhu X, Fu S, *et al.* Stabilizing high-entropy MAX phases by incorporating tin. *J Adv Ceram* 2025, **14**: 9221028.

[22] Wang S, Miao B, Nadeem MS, *et al.* Preparation and microwave absorption performance study of high-entropy MAX phase $(Ti_{1/4}V_{1/4}Zr_{1/4}Nb_{1/4})_2AlC$. *Ceram Int* 2025, **51**: 23760–71.

[23] Tan Y, Xia Y, Teng Z, *et al.* Synthesis and enhanced mechanical properties of compositionally

complex MAX phases. *J Eur Ceram Soc* 2021, **41**: 4658–65.

[24] Wei X, Li L, Liu F, *et al.* Synthesis, microstructure, and mechanical properties of MAX phase Ti_2GaC ceramics with V doping. *Ceram Int* 2024, **50**: 15806–20.

[25] Yang L, Cao Y, Gong Z, *et al.* First-principles calculations of the elastic anisotropy, thermal conductivity, and optical properties of MAX-phase M_2AlC (M = V, Nb, Ta) series carbides. *Vacuum* 2024, **230**: 113731.

[26] Zhao X, ElMeligy TA, Sokol M, *et al.* Effects of grain orientation and confinement on dynamic compressive behavior of highly oriented MAX phase Ta_2AlC. *Mech Mater* 2025, **207**: 105378.

[27] Liu L, Zhang M, Zhuang Q, *et al.* Mechanism-driven strengthening of MAX phase ceramics by $Ti_3C_2T_x$ MXene: A comparative study on Cr_2AlC and Ta_2AlC. *J Adv Ceram* 2025, **14**: 9221134.

[28] Toby BH, Von Dreele RB. *GSAS-II*: the genesis of a modern open-source all purpose crystallography software package. *J Appl Crystallogr* 2013, **46**: 544–9.

[29] Wang A, He Q, Liu C, *et al.* Microstructure and mechanical properties of boron carbide/graphene nanoplatelets composites fabricated by hot pressing. *Ceram Int* 2020, **46**: 7879–87.

[30] Zunger A, Wei SH, Ferreira LG, *et al.* Special quasirandom structures. *Phys Rev Lett* 1990, **65**: 353–6.

[31] Van De Walle A, Tiwary P, De Jong M, *et al.* Efficient stochastic generation of special quasirandom structures. *Calphad* 2013, **42**: 13–8.

[32] Giannozzi P, Baroni S, Bonini N, *et al.* QUANTUM ESPRESSO: a modular and open-source software project for quantum simulations of materials. *J Phys: Condens Matter* 2009, **21**: 395502.

[33] Giannozzi P, Andreussi O, Brumme T, *et al.* Advanced capabilities for materials modelling with Quantum ESPRESSO. *J Phys: Condens Matter* 2017, **29**: 465901.

[34] Perdew JP, Burke K, Ernzerhof M. Generalized Gradient Approximation Made Simple. *Phys Rev Lett* 1996, **77**: 3865–8.

[35] Grimme S, Antony J, Ehrlich S, *et al.* A consistent and accurate *ab initio* parametrization of

density functional dispersion correction (DFT-D) for the 94 elements H-Pu. *J Chem Phys* 2010, **132**: 154104.

[36] Momma K, Izumi F. *VESTA 3* for three-dimensional visualization of crystal, volumetric and morphology data. *J Appl Crystallogr* 2011, **44**: 1272–6.

[37] Deringer VL, Tchougréeff AL, Dronskowski R. Crystal Orbital Hamilton Population (COHP) Analysis As Projected from Plane-Wave Basis Sets. *J Phys Chem A* 2011, **115**: 5461–6.

[38] Maintz S, Deringer VL, Tchougréeff AL, *et al.* Analytic projection from plane-wave and PAW wavefunctions and application to chemical-bonding analysis in solids. *J Comput Chem* 2013, **34**: 2557–67.

[39] Maintz S, Deringer VL, Tchougréeff AL, *et al.* LOBSTER: A tool to extract chemical bonding from plane-wave based DFT. *J Comput Chem* 2016, **37**: 1030–5.

[40] Zhang L, Han J, Wang H, *et al.* Deep Potential Molecular Dynamics: A Scalable Model with the Accuracy of Quantum Mechanics. *Phys Rev Lett* 2018, **120**: 143001.

[41] Wang H, Zhang L, Han J, *et al.* DeePMD-kit: A deep learning package for many-body potential energy representation and molecular dynamics. *Comput Phys Commun* 2018, **228**: 178–84.

[42] Zeng J, Zhang D, Lu D, *et al.* DeePMD-kit v2: A software package for deep potential models. *J Chem Phys* 2023, **159**: 054801.

[43] Zhang L, Han J, Wang H, *et al.* End-to-end Symmetry Preserving Inter-atomic Potential Energy Model for Finite and Extended Systems. In: Advances in Neural Information Processing Systems, Curran Associates, Inc.; 2018.

[44] Zhang Y, Wang H, Chen W, *et al.* DP-GEN: A concurrent learning platform for the generation of reliable deep learning based potential energy models. *Comput Phys Commun* 2020, **253**: 107206.

[45] Thompson AP, Aktulga HM, Berger R, *et al.* LAMMPS - a flexible simulation tool for particle-based materials modeling at the atomic, meso, and continuum scales. *Comput Phys Commun* 2022, **271**: 108171.

[46] Zhao X, Sokol M, Barsoum MW, *et al.* Effect of grain orientation on the compressive response of highly oriented MAX phase Ti_3SiC_2. *Mater Sci Eng: A* 2021, **809**: 140869.

[47] Plummer G, Barsoum MW, Weinberger CR, *et al.* Basal dislocations in MAX phases: Core structure and mobility. *Materialia* 2022, **21**: 101310.

[48] Gavalda-Diaz O, Lyons J, Wang S, *et al.* Basal plane delamination energy measurement in a Ti_3SiC_2 MAX phase. *JOM* 2021, **73**: 1582 – 8.

[49] Fu X, Liang L, Wei Y. Characterization and Simulation of Nanoscale Catastrophic Failure of Metal/Ceramic Interfaces. *ACS Omega* 2023, **8**: 20313–22.

[50] Park K, Paulino GH. Cohesive Zone Models: A Critical Review of Traction-Separation Relationships Across Fracture Surfaces. *Appl Mech Rev* 2011, **64**: 060802.

[51] Stukowski A. Visualization and analysis of atomistic simulation data with OVITO–the Open Visualization Tool. *Model Simul Mater Sci Eng* 2010, **18**: 015012.

[52] He G, Zhang Y, Yao P, *et al.* A novel medium-entropy $(TiVNb)_2AlC$ MAX phase: Fabrication, microstructure, and properties. *J Mater Sci Technol* 2023, **137**: 91–9.

[53] Wang K, Chen L, Xu C, *et al.* Microstructure and mechanical properties of (TiZrNbTaMo)C high-entropy ceramic. *J Mater Sci Technol* 2020, **39**: 99–105.

[54] Chen D, Shirato K, Barsoum MW, *et al.* Cyclic Fatigue-Crack Growth and Fracture Properties in Ti_3SiC_2 Ceramics at Elevated Temperatures. *J Am Ceram Soc* 2001, **84**: 2914–20.

[55] Gilbert CJ, Bloyer DR, Barsoum MW, *et al.* Fatigue-crack growth and fracture properties of coarse and fine-grained Ti_3SiC_2. *Scr Mater* 2000, **42**: 761–7.

[56] Zhang Y, Zhou YJ, Lin JP, *et al.* Solid-solution phase formation rules for multi-component alloys. *Adv Eng Mater* 2008, **10**: 534–8.

[57] Magnuson M, Mattesini M. Chemical bonding and electronic-structure in MAX phases as viewed by X-ray spectroscopy and density functional theory. *Thin Solid Films* 2017, **621**: 108–30.

[58] Magnuson M, Näslund LÅ. Local chemical bonding and structural properties in Ti_3AlC_2 MAX

phase and $Ti_3C_2T_x$ MXene probed by Ti 1*s* x-ray absorption spectroscopy. *Phys Rev Res* 2020, **2**: 033516.

[59] Leguillon D, Martin É, Lafarie-Frenot MC. Flexural vs. tensile strength in brittle materials. *C R, Méc* 2015, **343**: 275–81.

[60] Ghaffari K, Bavdekar S, Spearot DE, *et al.* Validation workflow for machine learning interatomic potentials for complex ceramics. *Comput Mater Sci* 2024, **239**: 112983.

[61] Wen T, Wang R, Zhu L, *et al.* Specialising neural network potentials for accurate properties and application to the mechanical response of titanium. *Npj Comput Mater* 2021, **7**: 206.

[62] Lin S, Casillas-Trujillo L, Tasnádi F, *et al.* Machine-learning potentials for nanoscale simulations of tensile deformation and fracture in ceramics. *Npj Comput Mater* 2024, **10**: 67.

[63] Terban MW, Billinge SJL. Structural Analysis of Molecular Materials Using the Pair Distribution Function. *Chem Rev* 2022, **122**: 1208–72.

[64] Dai FZ, Wen B, Sun Y, *et al.* Theoretical prediction on thermal and mechanical properties of high entropy $(Zr_{0.2}Hf_{0.2}Ti_{0.2}Nb_{0.2}Ta_{0.2})C$ by deep learning potential. *J Mater Sci Technol* 2020, **43**: 168–74.

[65] Dai FZ, Sun Y, Wen B, *et al.* Temperature Dependent Thermal and Elastic Properties of High Entropy $(Ti_{0.2}Zr_{0.2}Hf_{0.2}Nb_{0.2}Ta_{0.2})B_2$: Molecular Dynamics Simulation by Deep Learning Potential. *J Mater Sci Technol* 2021, **72**: 8–15.

[66] Dandekar CR, Shin YC. Molecular dynamics based cohesive zone law for describing Al–SiC interface mechanics. *Compos A: Appl Sci Manuf* 2011, **42**: 355–63.

[67] Sangiovanni DG, Tasnádi F, Harrington T, *et al.* Temperature-dependent elastic properties of binary and multicomponent *high-entropy* refractory carbides. *Mater Des* 2021, **204**: 109634.

[68] Steneteg P, Hellman O, Vekilova OYu, *et al.* Temperature dependence of TiN elastic constants from *ab initio* molecular dynamics simulations. *Phys Rev B* 2013, **87**: 094114.

[69] Mozafari E, Shulumba N, Steneteg P, *et al.* Finite-temperature elastic constants of paramagnetic

materials within the disordered local moment picture from *ab initio* molecular dynamics calculations. *Phys Rev B* 2016, **94**: 054111.

[70] Xiang H, Feng Z, Li Z, *et al.* First-principles investigations on elevated temperature elastic and thermodynamic properties of ZrB_2 and HfB_2. *J Am Ceram Soc* 2017, **100**: 3662–72.

[71] George J, Petretto G, Naik A, *et al.* Automated Bonding Analysis with Crystal Orbital Hamilton Populations. *ChemPlusChem* 2022, **87**: e202200123.

[72] Müller PC, Reitz LS, Hemker D, *et al.* Orbital-based bonding analysis in solids. *Chem Sci* 2025, **16**: 12212–26.

[73] Liu Y, Xie X, Liu Z, *et al.* Strong and tough magnesium-MAX phase composites with nacre-like lamellar and brick-and-mortar architectures. *Commun Mater* 2023, **4**: 30.

[74] Gavalda-Diaz O, Saiz E, Chevalier J, *et al.* Toughening of ceramics and ceramic composites through microstructure engineering: A review. *Int Mater Rev* 2025, **70**: 3–30.

[75] He Z, Chen K, Li Z, *et al.* Structural editing of MAX phases for high-toughness ceramics. *J Eur Ceram Soc* 2026, **46**: 118388.

[76] Janssen M, Zuidema J, Wanhill R. Fracture Mechanics: Fundamentals and Applications. 2nd ed. London, CRC Press; 2004.

[77] Ranganathan SI, Ostoja-Starzewski M. Universal elastic anisotropy index. *Phys Rev Lett* 2008, **101**: 055504.